An experimental and numerical study of droplet motion and enhanced condensation due to mechanical vibrations

by

Ryan Andrew Huber

B.S., Kansas State University, 2016

AN ABSTRACT OF A DISSERTATION

submitted in partial fulfillment of the requirements for the degree

DOCTOR OF PHILOSOPHY

Alan Levin Department of Mechanical and Nuclear Engineering
Carl R. Ice College of Engineering

KANSAS STATE UNIVERSITY
Manhattan, Kansas

2021

Abstract

The Energy-Water nexus is devoted to studying how to reduce the amount of water consumption needed to produce power. In 2010, the U.S. energy production accounted for 40% of freshwater withdrawals and 3% of freshwater consumption [1]. This research focuses on reducing the amount of drift loss from evaporative cooling towers at power plants by condensing the drift loss while it is inside the cooling tower, so it may be collected and reused or recycled in the area. Ghosh et al. [2] used a simple mesh screen in order to collect 40% of the drift loss. This research studies the impacts of vibrations on droplet shedding during condensation; the sooner droplets depart from the condensing surface, the higher the rate of heat transfer [3, 4].

This research focuses on understanding the fundamentals of the droplets motion on a vertical hydrophobic surface in order to determine how to best utilize vibrational forces in order to shed the droplets as fast as possible. Visualization studies examined the droplet modes of 3-μL water droplets at three different vibration settings (i.e., 30 Hz, 70 Hz, and 100 Hz). The resulting modes that were observed were rocking (i.e., no droplet slip), ratchet (i.e., droplet slipping), and ejection (i.e., detaching from the surface). In addition to filtered and de-ionized (DI) water, three other water samples (e.g., simulated salt, flue gas desulfurization, and cooling tower blowdown) were tested in this manner in order to determine how the water properties affected the droplet modes. Numerical studies using the lattice Boltzmann method were validated against experimental results. Numerical studies of the de-ionized water droplets allowed for uncoupling of the vibrational directions, showing that vibrational forces in the direction of gravity played the most important role in droplet shedding. The numerical studies also allowed for test cases that were difficult to accomplish with the experimental apparatus to be conducted. Visual condensation tests showed that the vibrations allowed for droplets to begin shedding earlier (i.e.,

20 minutes on vibrating compared to 110 minutes on stationary surfaces) and at smaller diameters (e.g., 1 mm vs 5 mm).

Experiments were conducted in an environmental chamber at 40 °C and 60% RH. Inside this chamber, condensation heat transfer experiments were conducted on stationary and vibrating hydrophobic surfaces. The condensation heat transfer coefficients of moist air measured in these experiments ranged from 100 to 150 W/m^2K, with the average stationary heat transfer coefficient of 120 W/m^2K and the average vibrating heat transfer coefficient of 130 W/m^2K. Although the measured difference is modest, it shows that there is a possibility of this being a viable method to enhance condensation heat transfer. Further work is needed to improve the condensation rate of the apparatus in order to better understand the impacts and improvements vibrations have on the heat transfer coefficient.

An experimental and numerical study of droplet motion and enhanced condensation due to mechanical vibrations

by

Ryan Andrew Huber

B.S., Kansas State University, 2016

A DISSERTATION

submitted in partial fulfillment of the requirements for the degree

DOCTOR OF PHILOSOPHY

Alan Levin Department of Mechanical and Nuclear Engineering
Carl R. Ice College of Engineering

KANSAS STATE UNIVERSITY
Manhattan, Kansas

2021

Approved by:

Major Professor
Melanie M. Derby

Copyright

Abstract

The Energy-Water nexus is devoted to studying how to reduce the amount of water consumption needed to produce power. In 2010, the U.S. energy production accounted for 40% of freshwater withdrawals and 3% of freshwater consumption [1]. This research focuses on reducing the amount of drift loss from evaporative cooling towers at power plants by condensing the drift loss while it is inside the cooling tower, so it may be collected and reused or recycled in the area. Ghosh et al. [2] used a simple mesh screen in order to collect 40% of the drift loss. This research studies the impacts of vibrations on droplet shedding during condensation; the sooner droplets depart from the condensing surface, the higher the rate of heat transfer [3, 4].

This research focuses on understanding the fundamentals of the droplets motion on a vertical hydrophobic surface in order to determine how to best utilize vibrational forces in order to shed the droplets as fast as possible. Visualization studies examined the droplet modes of 3-μL water droplets at three different vibration settings (i.e., 30 Hz, 70 Hz, and 100 Hz). The resulting modes that were observed were rocking (i.e., no droplet slip), ratchet (i.e., droplet slipping), and ejection (i.e., detaching from the surface). In addition to filtered and de-ionized (DI) water, three other water samples (e.g., simulated salt, flue gas desulfurization, and cooling tower blowdown) were tested in this manner in order to determine how the water properties affected the droplet modes. Numerical studies using the lattice Boltzmann method were validated against experimental results. Numerical studies of the de-ionized water droplets allowed for uncoupling of the vibrational directions, showing that vibrational forces in the direction of gravity played the most important role in droplet shedding. The numerical studies also allowed for test cases that were difficult to accomplish with the experimental apparatus to be conducted. Visual condensation tests showed that the vibrations allowed for droplets to begin shedding earlier (i.e.,

20 minutes on vibrating compared to 110 minutes on stationary surfaces) and at smaller diameters (e.g., 1 mm vs 5 mm).

Experiments were conducted in an environmental chamber at 40 °C and 60% RH. Inside this chamber, condensation heat transfer experiments were conducted on stationary and vibrating hydrophobic surfaces. The condensation heat transfer coefficients of moist air measured in these experiments ranged from 100 to 150 W/m^2K, with the average stationary heat transfer coefficient of 120 W/m^2K and the average vibrating heat transfer coefficient of 130 W/m^2K. Although the measured difference is modest, it shows that there is a possibility of this being a viable method to enhance condensation heat transfer. Further work is needed to improve the condensation rate of the apparatus in order to better understand the impacts and improvements vibrations have on the heat transfer coefficient.

Table of Contents

List of Figures

List of Tables

Acknowledgements

I would like to thank Dr. Melanie Derby for being my major professor. It is because of her insights and willingness to lend a helping hand that I was able to enjoy my time in graduate school and learn so much. I would also like to express my gratitude towards Dr. B. Terry Beck, Dr. Amy Betz, and Dr. Hutchinson for their guidance on my research project and being members of my committee. Their expertise was extremely helpful to the completion of various parts of my research. I want to thank Matt Campbell for his help in finding and explaining an excellent simulation software that suited my project perfectly. Not even to mention the tremendous help he has been while I have been working in IER.

I would like to thank IER for their great hospitality allowing me to work in their environmental chambers as well as all the various equipment they have lent over the years. I would like to thank NSF for funding this project with grant 1603737.

I would also like to thank my undergraduate assistants for their help in data collection and construction. Also, a special shout out to Nicole Doughramaji for her help with running experiments, analyzing videos, and stitching together all the simulation photos into videos.

Finally, I would like to thank my friends, family, and especially my lab mates for their support and help with making sure I took time to relax as well.

Chapter 1 - Introduction and Literature Review

1.1 Motivation

In the Energy-Water nexus power production is a particular interest since it is currently responsible for withdrawing over 500 billion liters of freshwater per day and consuming 3% of all freshwater in the U.S [1, 5]. While there are advances being made in enhancing air-cooling for power production, air cooling is not able to reproduce the productivity of water-cooling, because air has a lower volumetric specific heat (1.2 kJ/m^3K) than the latent heat of vaporization of water (2,252,000 kJ/m^3). Therefore, the current approach is to reduce the amount of water used in evaporative cooling towers. One approach is to capture or re-condense evaporated water, without using a significant amount of power [2]. This dissertation will look at enhancing dropwise condensation via vibrations. The hypothesis is that the vibrations will promote droplet shedding and increase the amount of water that can be reclaimed from the cooling towers.

1.2 Previous Cooling Tower Research

Condensers in thermo-electric power plants (e.g., coal, natural gas, nuclear, and concentrated solar power plants [6, 7]) require adequate cooling to maintain plant operation at high cycle thermal efficiencies. Wet cooling towers utilize the latent heat of evaporation of water to cool, while dry cooling towers utilize ambient air. The wet cooling towers use water to cool the steam to a desired temperature, but evaporates 2500 gal/MWh on average. Average water consumption by power plant type is shown in Table 1.1[6, 7].

Table 1.1: Average water consumption for different power generations wet cooling towers [6, 7]

Power Plant Type	Consumption [L/MWh]
Coal	2350
Natural Gas	1700
Nuclear	2650
Concentrated Solar	3220

Typical air-cooling towers have an average performance deficit of 6% compared to evaporative cooling towers because the dry cooling towers are not able to cool the steam to as low of a temperature as wet cooling towers, leading to a higher back pressure on the turbines and lower performance [8]. There are numerous disadvantages to air-cooling, including ambient wind effects and hot day penalty [9-12]. The hot day penalty is a major factor in the decreased performance for air-cooling due to the decrease in temperature difference in ambient air and the steam (e.g., on days when air temperatures exceed 30^{o}C). This can result in a decrease in power generation of 8%-25% on a hot day by increasing the turbine back pressure [5]. For dry cooling towers to be competitive with wet cooling towers in terms of performance, the airflow rates need to be increased by 68% and convective heat transfer resistances need to be decreased by 66% while maintaining the pressure losses at 25% [8]. This is a challenge for dry cooling towers, but hybrid cooling combines some of the advantages of dry cooling and wet cooling; having some cooling from each of the two types of towers, a 50-50 split was found to decrease the performance of air-cooling by 1.67% while only using 48% of the water as wet cooling [13] .

Another option is spray a cooling mist or used a wetted media to cool the air before it passes over the condensers [9, 14-23].

Due to the high thermal performance of wet cooling towers, collecting evaporated water from wet cooling towers is an active research topic. Ghosh et al. [2] utilized fog collectors – simple devices that in capturing potable water from foggy places with limited sources of water. Since wet cooling towers are known for creating clouds it stands to reason that the fog collectors would be very useful in capturing the water that is lost. Ghosh et al. [2] have had some success in implementing this technology in actual power plant cooling towers. The study placed wire meshes inside a 500 MW power plant wet cooling tower and was able to reclaim 40% of the drift loss, 54 L/m^2 of mesh [2].

1.3 Droplet Motion Due to Vibrations

1.3.1 Physics

Droplet motion physics is a complex issue which has been studied numerically and experimentally [24-26]. To be able to better understand the physics during vibration, it is important to first understand the physics of a droplet on a non-vibrating surface.

1.3.1.1 Stationary Surfaces

Droplets on an inclined or, as shown in Figure 1.1, a vertical surface have two primary forces acting on them: the gravitational force (F_g) and capillary force (F_C) [26]. The equations for these forces are Eq. 1.1 and Eq. 1.2 respectively.

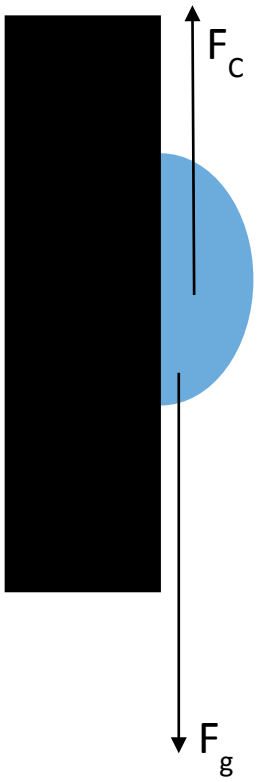

Figure 1.1 Droplet on a stationary surface force diagram

$$F_g = \rho V g \qquad \textbf{Eq. 1.1}$$

$$F_C = \pi r \gamma (\cos\theta_r - \cos\theta_a) \qquad \textbf{Eq. 1.2}$$

Where ρ is liquid density, V is volume, g is gravity, r is radius, γ is surface tension, θ_r is receding contact angle, and θ_a is advancing contact angle. On a stationary surface, the gravitational force is the driving force and must overcome the capillary forces. If the droplet is not moving then the capillary force is in balance with the gravitational force. If the gravitational force is greater than the maximum capillary force, then the droplet will begin to move. Since both forces are functions of droplet radius, and the advancing and receding angles can only change so much, there exists a radius in which the gravitational force become larger than the capillary force.

1.3.1.2 Vibrating Surfaces

When the surface is vibrated underneath the droplet, the force diagram becomes more complex, as shown in Figure 1.2. The vibration adds two internal forces that change the shape of the drop and its contact angles: inertial forces from the water swirling around and Laplace pressure forces, which are trying to force the droplet back to its resting state [25].

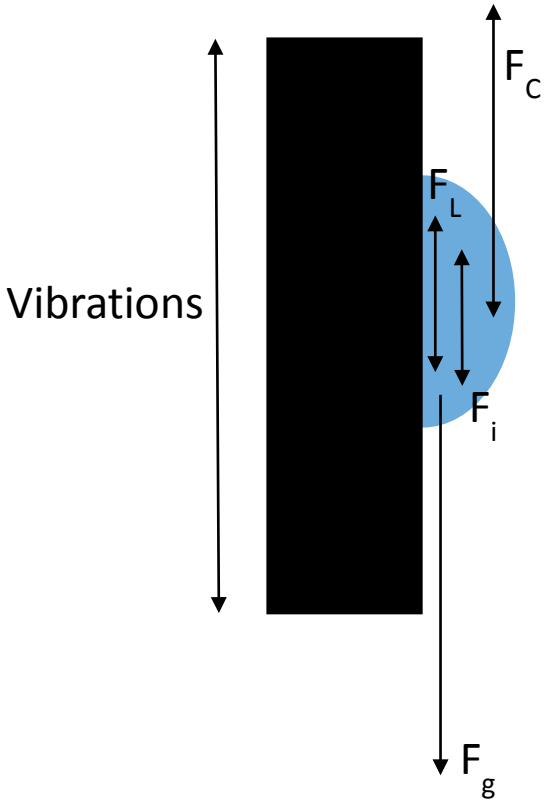

Figure 1.2: Droplet on a vibrating surface force diagrams

Eq. 1.2 indicates that the capillary force can change and even reverse as the droplet is deformed and contact angles change. Additionally, the capillary force can also be eliminated if the droplet has the same advancing and receding angles. For the brief time period that the droplet is deformed to this state, the gravitational force needed to move the droplet is reduced.

1.3.2 Experiments

Experimental and numerical studies have been done to better understand the complexities that arise during vibration induced droplet motion [27]. Dong et al. [27] experimentally

validated CFD simulations to show that there are multiple resonance modes for the same droplet. The first mode has been classified as the rocking mode in which the deformation to the droplet is not significant and it simply appears to be rocking back and forth. The second, third, and fourth modes are classified as the Rayleigh first, second, and third modes. These modes are distinguished by the different number of deformation nodes that are present on the droplet surface, with the second mode having two nodes and the third and fourth mode having three and four nodes respectively. While this work was not done on an inclined surface, the droplet resonance modes have been observed on a vertical surface as well [My paper]. They also did not observe any droplet movement along the lateral surface.

When it comes to droplet movement along the substrate, studies demonstrated that it is possible to direct the droplet to move in a certain direction and even uphill against gravity [24, 28]. Mettu and Chaudhury [28] directed droplet motion on a lateral surface with vibrations parallel to the plate. For a given amplitude and frequency, it was possible to overcome an 8° contact angle hysteresis, but not a 23° hysteresis. It was also necessary for some amount of hysteresis greater than 2° to exist as no motion was observed on that surface. They also found that different volumes of water behaved differently when undergoing the same vibrational mode. A 4-μL droplet was able to climb a 15° inclined surface, while a 1 μL droplet slid down the inclined surface. Brunet et al. [24] mapped droplet motion, indicating if a 5 μL droplet would climb, slide, or stick to an inclined surface of 45°. This map is shown in Figure 1.3, where the orange section is climbing, the blue section is sliding, and the white sections are static. As can be seen the larger the acceleration at a given frequency the droplet will climb the surface rather than slide. The droplet will climb the surface at a much higher frequency compared to sliding, but the large accelerations remain necessary.

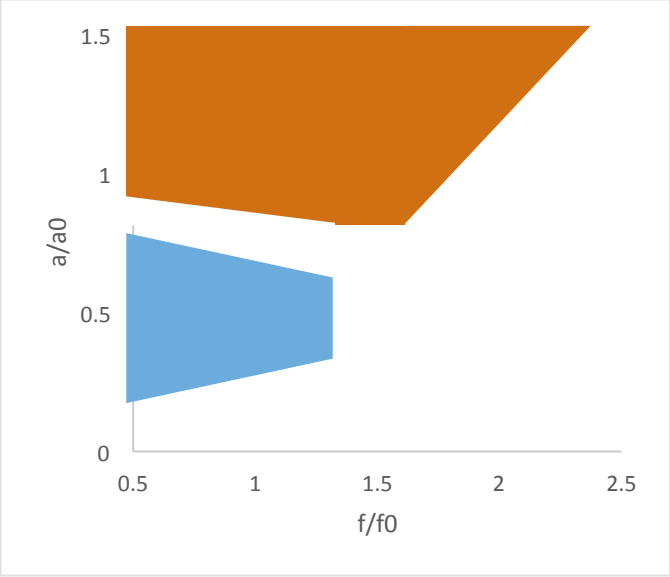

Figure 1.3: Droplet motion zones with normalized frequency and acceleration f_0 = 50.77 Hz a_0 = 174 m^2/s [24]

1.4 Condensation

Condensation has two modes, filmwise and dropwise. Filmwise condensation occurs when the condensing surface has high surface energy (i.e., hydrophilic) and the water is able to spread out and form a thin liquid film. In dropwise condensation, the phenomenon is caused by a low surface energy (i.e., hydrophobic) material and allows the water to form small droplets on the surface. Filmwise condensation is substantially less efficient (e.g., often by an order of magnitude) compared to dropwise condensation due to the thermal resistance that is created by the thin liquid films. As the water droplets grow during dropwise condensation, the growing droplets also create a thermal resistance, though not as large as during filmwise [29]. If water is condensing on an inclined surface eventually the droplets will grow large enough to depart, ~2 mm, from the surface [3, 4, 30]. As these droplets depart they coalesce with any droplets on their path below them taking them with clearing more area. Once this occurs, the cycle can begin again [31, 32].

The first stage of dropwise condensation is nucleation and can occur in two different ways, heterogeneous or homogenous [33] . Homogenous nucleation occurs on a completely flat surface where the droplets have no preference of forming, while heterogeneous nucleation occurs when there are small imperfections on the surface that are more desirable for nucleation to occur[33]. Barati et al. [33] found that as the difference in ambient temperature and condensing surface temperature became larger, smaller nucleation sites become active thus increasing the nucleation density of water droplets on the surface. For these cases, while this did increase the total heat transfer of the plate it did not increase the heat transfer coefficient [33]. Not only do surface imperfections affect nucleation, but the surface material does as well. Sokuler et al. [34] found that nucleation occurred faster on soft surfaces due to the droplets ability to deform the surface. Since dropwise condensation require condensing surfaces to have low surface energy, many condensing surfaces have to be coated in a promoter in order to achieve dropwise condensation. Mu et al. [35] found that the application method of this promoter can also impact the nucleation stage. Nucleation just does not occur at the beginning stages of condensation, it is a continuous process that occurs many times throughout the dropwise condensation process wherever there is free space [32, 33]. Leach et al. [32] found that impurities left behind by previously condensed water can cause sections of the surface to not have any nucleation, or no grow zones.

After nucleation occurs water droplets, begin to grow due to direct condensation. This growth is in accordance with the power law in Eq. 1.3 where R is droplet radius, t is time, and n is a variable power [31, 36].

$$R \sim t^n \qquad \textbf{Eq. 1.3}$$

The exponent in the power law can be increased by an increase in relative humidity. This means that droplets can grow faster at higher relative humidities [31]. Another factor in the growth rate is a droplet's proximity to other droplets. Leach et al. found this is only a problem when new droplets nucleate in areas that have been cleared due to either droplet departure or coalescence. The larger droplets are able to diffuse more of the water vapor from the air than the smaller droplets, leading to a slower growth rate [32]. Not only do these larger droplets slow the growth of new droplets, they can also hinder the nucleation on new droplets up to 50 μm away. These no growth zones can be smaller at higher temperatures [32]. Once the droplets reach three to four times the radius of the smallest viable drop, shown in Eq. 1.4 , they no longer grow primarily due to condensation because of the thermal resistance of the droplets [37] and primarily grow due to coalescence (i.e., one or more droplets merges to form a much larger droplet).

$$\check{r} = \frac{2\gamma v_f T_v}{h_{fg}\Delta T} \qquad \textbf{Eq. 1.4}$$

where $\check{r}$ is the radius of the smallest viable drop, γ is the surface tension of water, v_f is the specific volume of water, T_v is the vapor temperature, h_{fg} is the latent heat of vaporization of water, and ΔT is the vapor to surface temperature difference. Coalescence causes a step change in the growth of the droplet, as the size of the droplets grow substantially larger than during direct condensation [36]. The massive step change that occurs when droplets merge dominates the growth rate of an individual droplet; as a result, the growth rate of droplets once coalescence dominates is independent of relative humidity [31]. Sokuler et al. [34] found that soft surfaces impede the speed at which droplets are able to coalesce. On an inclined or vertical surface, the droplets will reach a critical diameter in which the force of gravity is able to overcome the surface pinning forces and the droplet will slide off the surface [3, 4, 37]. According to Rose [37] at atmospheric pressure a good estimate for this critical diameter is 2 mm on a vertical surface.

Lee et al. [4] found that more hydrophobic surfaces with larger contact angles, 148° versus 124°, decreased the time it took for the critical diameter to be reached on a vertical surface by 30 minutes. This increase led to a 1.5 times larger heat flux for a surface with a contact angle of 148° vs a surface with a contact angle of 124° [4]. Dietz et al. [3] reduced critical droplet diameters to 0.25 mm found on a super hydrophobic surface, thereby improving estimated heat transfer coefficients by 100% compared to Rose's [29] estimate using 2 mm as the critical diameter.

Once a droplet has departed a condensing surface, the previous area it occupied and the area in its path of departure are able to nucleate new droplets, as long as they are not in no-grow zones [31, 32]. This is a major advantage for dropwise condensation, since this not only removes the thermal resistance from many droplets but also allows small droplets to form again. This is beneficial since small droplets, $< 3\breve{r}$, are the primary source of direct condensation [31]. Since the latent heat of vaporization of water is so high, 2,206 kJ/kg at standard temperature and pressure, direct condensation is the primary driver of heat transfer in this process.

1.5 Research Objectives

The main objective of this research is to determine and understand the effect vibrations have on a condensing surface and the condensation heat transfer. This will be done through four main steps:

1. Investigate droplet motion on vertical surfaces due to vibrations.
2. Determine whether the lattice Boltzmann method can capture vibration induced droplet physics.
3. Determine the impact vibrations have on droplet shedding during condensation.
4. Determine the impact vibrations have on condensation heat transfer

Chapter 2 - Experimental Apparatus

2.1 Experimental Apparatus

Over the course of this research, there were two main iterations of experimental apparatus to study droplet motion and condensation. The first was an aluminum frame with flexible material stretched taunt across it to test different types of materials and their droplet shedding capabilities. After testing Teflon film, silver foil, and two wire meshes, the Teflon film was selected for further investigation as it was the only one that had droplet motion. This apparatus was used to visualize water droplet motion and condensation experiments. The second apparatus was a 3D-printed heat exchanger with a Teflon-coated aluminum plate used to measure the heat transfer rate of condensation.

2.1.1 Visual Apparatus

The visual experimental apparatus was built using a 0.61-m by 0.61-m aluminum frame attached via a pivot to a large steel frame in order to keep most of the vibrational force in the frame. Vibrations were created by using an eccentric mass (i.e., a brass sprocket with three 4.37 mm holes drilled into one section) attached to a brushless DC motor and bolted to the bottom of the aluminum frame. After testing the efficacy of droplet shedding, while stationary and vibrating a 0.254-mm-thick Teflon film was tensioned to 41.4 kPa across the aluminum frame. This film worked best because it is a hydrophobic material and has a stationary contact angle of 105°; this allowed for smaller droplets to form and shed easier than on the other surfaces where the vibrations just expanded the surface area of the droplet. For visualization of these experiments a high-speed camera was used to capture the droplet motions.

2.1.1.1 Droplet Motion

The apparatus for droplet shedding experiments can be seen in Figure 2.1, 2-µL droplets were placed onto the Teflon film using a pipette. The high speed camera was placed off to the side so the contact line motion of the droplet could be observed. Using a DC power supply, three voltages were applied to the motor to create three different vibrational modes. These voltages were 4.4, 8, and 12 V. Each of these corresponded to a different vibrational frequency, which was measured with a laser vibrometer, corresponding to frequencies of 30, 60, and 100 Hz, respectively.

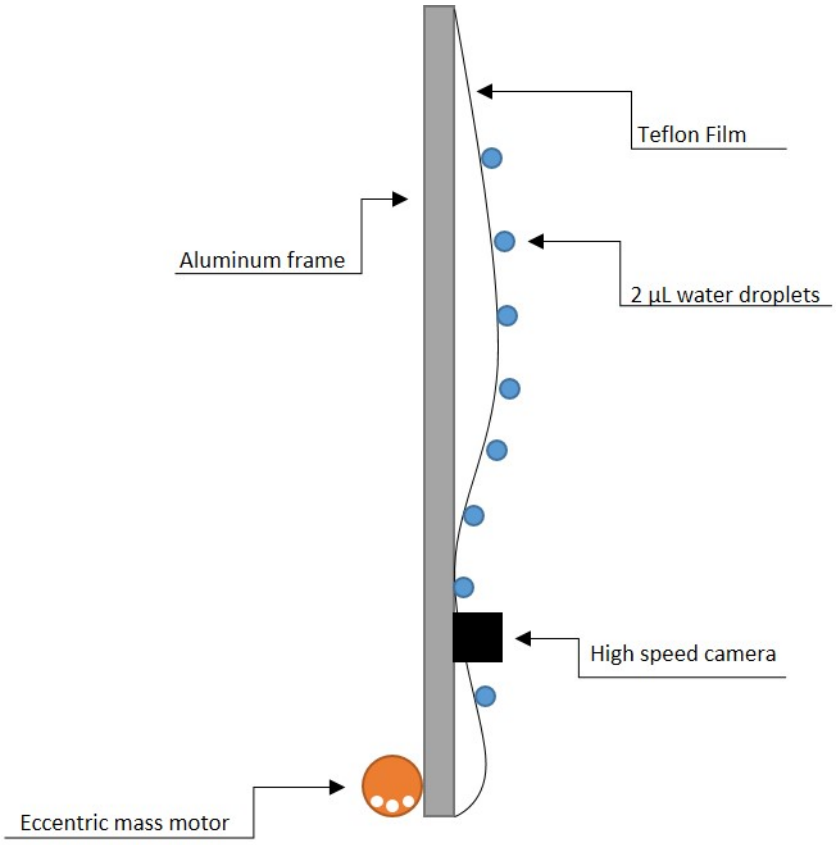

Figure 2.1: Apparatus for viewing individual water droplet motion

Research was also conducted to determine if water quality had any impact on droplet motion. Four different water qualities were tested; deionized and filtered (DI) water, cooling

tower blowdown (CTB) water, flue gas desulfurization (FGD) water, and simulated salt water. The water properties and composition are provided in the tables below [38, 39].

Table 2.1: Table of liquid material properties for four different water qualities [38]

Property	DI	Salt	CTB	FGD
Density (kg/m^3)	998.4	1033.1	1007.1	1014.5
Viscosity (cp)	1.002	1.223	1.065	1.115
Surface Tension (mN/m)	72.81	64.78	71.58	69.16

Table 2.2: Table of chemical composition for two different water qualities [39]

	EC	**pH**	**S**	**K**	**Na**	**Mg**	**Ca**	**Chloride**	**NO3-N**	**NH4-N**
	(dS/m)		(mg/L)							
CTB	1	8.9	105	42	186	70	111	221	1	0
FGD	6.6	7	904	220	1395	0	810	2038	32	5

2.1.1.2 Condensation

For condensation tests the apparatus can be seen in Figure 2.2, an environmental chamber was used to control the temperature (± 0.2°C) and humidity (±2% RH) of the ambient air. A cooled air stream was blown onto the back of the Teflon film to lower the temperature of the surface to promote condensation. The surface temperature and cool air temperature was measured using type T thermocouples (± 0.2°C). The cool air was supplied by running compressed air through a hose submerged in a bucket of ice or a chiller. The condensation was monitored from the front of the condensing surface and at the top of the condensing area to be able to determine the critical departure diameter of the droplets. Ambient conditions in the chamber ranged from 30°C– 35°C and 50% – 66% RH.

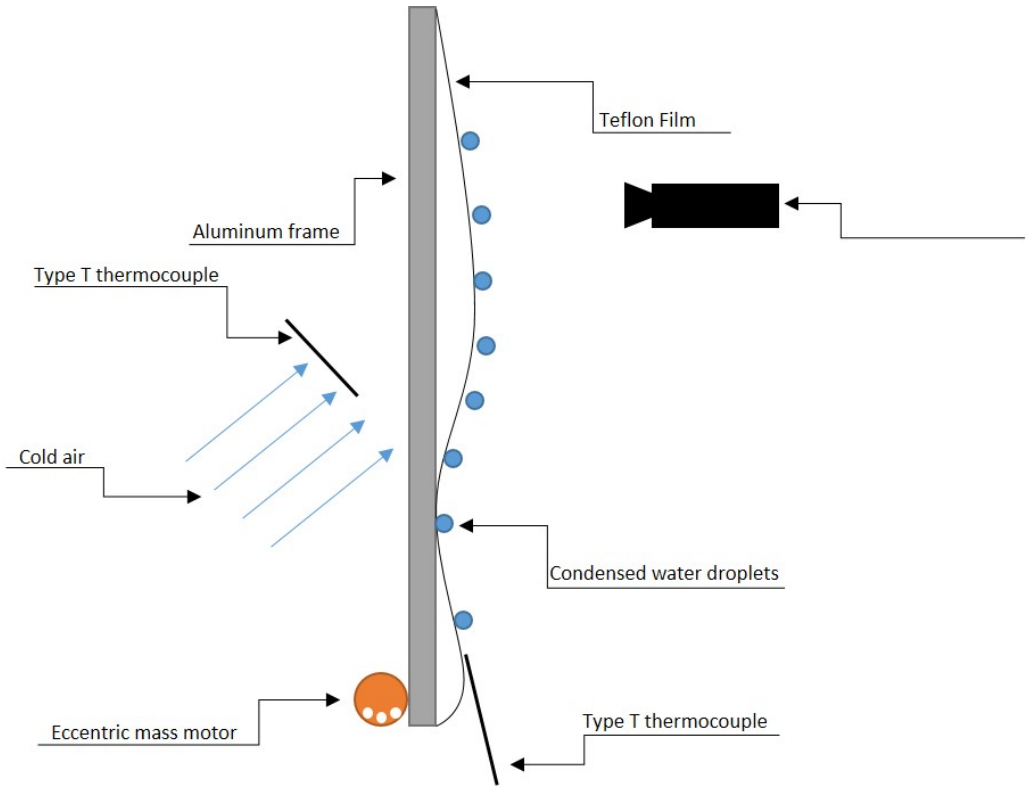

Figure 2.2: Apparatus for viewing droplet motion during water condensation

2.1.2 Heat Transfer Apparatus

The heat transfer apparatus, shown in Figure 2.3, is a 3D-printed plastic heat exchanger with a Teflon-coated aluminum condensing plate glued to the front and sealed with silicon. The 3D printed part consists of a single inlet for cold air supply, two straighteners to promote even air flow, and five 28.88 wide and 152.4 mm long channels. The inlet temperature is measured at the start of each channel in the 3D printed part, the outlet temperatures are measured 0.6 m after the end of each 3D printed channel to ensure mixing of the airflow so bulk temperature can be measured. The entire 3D printed part and all tubes attached to it are insulated so that the losses are minimal and heat transfer on the condensing surface dominates, but still considered in the heat transfer coefficient calculations. A new eccentric mass was created with the same center of eccentricity and was slid into a compartment in the back designed to hold the motor. Two 3 wire

RTD's were placed in opposite corners of the condensing surface to measure the temperature of the plate.

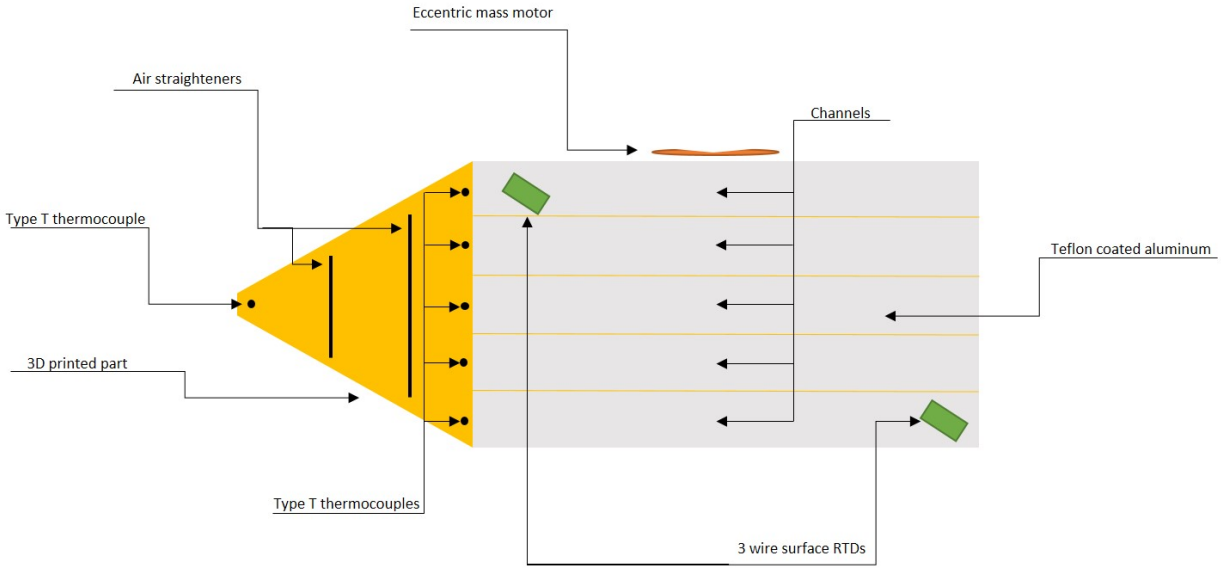

Figure 2.3: Apparatus for measuring condensation heat transfer coefficients of moist air

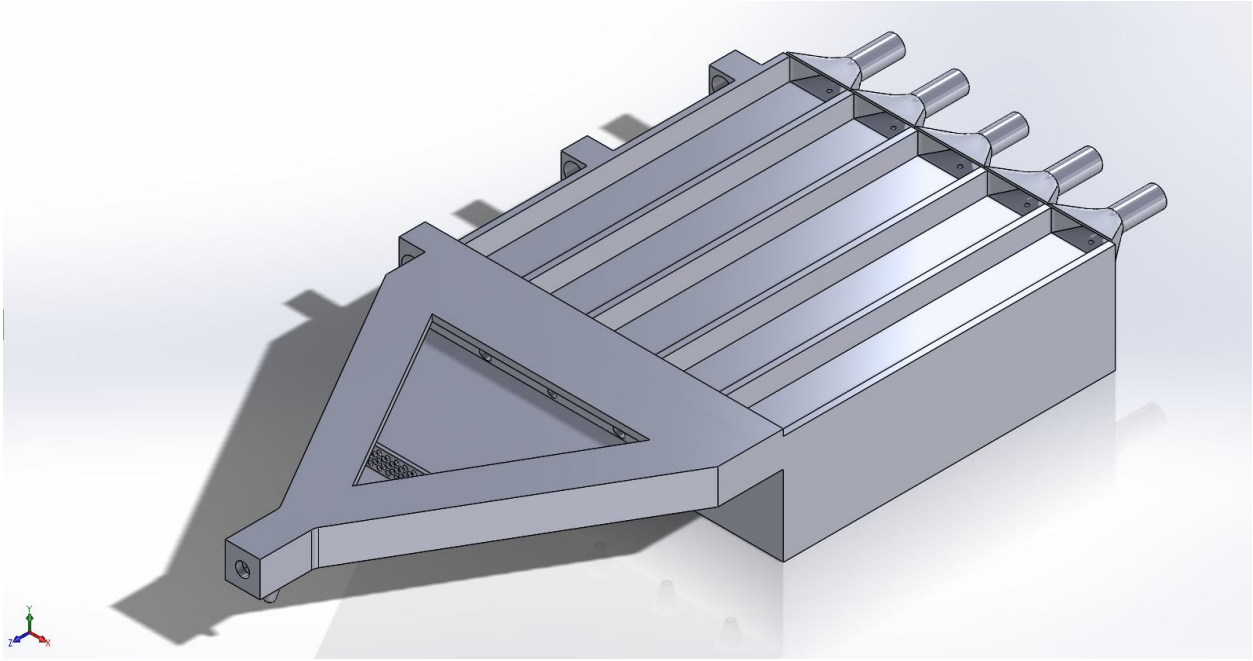

Figure 2.4 CAD model of apparatus for measuring condensation heat transfer coefficients of moist air

To create condensation, the apparatus was placed in an environmental chamber and set to 40 °C and maximum humidity for the chamber at this temperature, around 60% RH. The ambient air temperature and dew point were measured with a type T thermocouple and a dew point hydrometer, ±0.1 °C, respectively. Cold air was supplied by running compressed air through a copper coil submerged in a chiller set to 5 °C. The air ran along the back side of the Teflon coated aluminum plate and lowered its temperature below the dew point. Moist air was blown upward along the condensing surface at a rate of 4 m/s. Condensed water was collected in a tray under the plate as it departed so it can be measured after the test, ±1 mL. Temperature measurements were collected for an hour after steady state was reached to determine the heat transfer and heat transfer coefficient.

2.2 Equations and uncertainty

2.2.1 Droplet Motion

On the droplet shedding apparatus the average velocity, u, of an individual droplet was calculated, Eq. 2.1, as it moved past the camera lens. Uncertainties were determined by counting the number of frames it took the droplet to come into view and then leave view to calculate the elapsed time, Δt. The vertical distance that the view covered, Δx, was measured using the known pixel size of the camera. This provides a distance uncertainty, δ_x, of 14 μm and a time uncertainty, δ_t, of 2 ms. These can be used in Eq. 2.2 to solve for the uncertainty of the average velocity, where t is time and x is distance.

$$\bar{u} = \frac{\Delta x}{\Delta t} \qquad \textbf{Eq. 2.1}$$

$$\delta_{\overline{u}} = \sqrt{{\delta_x}^2 t^{-2} + \left(\frac{-x}{t^2}\right)^2 {\delta_t}^2} \qquad \textbf{Eq. 2.2}$$

2.2.2 Condensation

For the visual condensation experiments, the time for a droplet to shed was found using the time stamp on the video when a droplet started departing, the uncertainty of which is negligibly small. The diameter of the droplet before departure was measured using software and calibrated using a ruler in the video. The uncertainty of these measurements was 0.1 mm.

2.2.3 Heat Transfer

The temperature measurements were saved to .csv files and processed using a Matlab program. To calculate the average heat transfer from the cold air, the average difference in each channels exit temperature and inlet temperature, $T_{exit} - T_{inlet}$, was multiplied by mass flow rate, *m dot*, and the specific heat, c_p. This is what is shown in Eq. 2.3 where n is the number of data points measured. The uncertainty for this measurement is shown in Eq. 2.4 where δ_{thermo} is the uncertainty of the type T thermocouples, 0.2 °C, and δ_m is the uncertainty of the mass flow rate, 0.00003 kg/s. The heat loss and its uncertainty are calculated using Eq. 2.5 and Eq. 2.6 respectively. Where the temperature difference is the average air temperature in the channels and A_{loss} is the surface area besides the condensing surface, the back of the apparatus and the tubing after the heat transfer section before the exit thermocouples, and δ_A is the error of the surface area. Eq. 2.7 and Eq. 2.8 are how to calculate the heat transfer due to conduction; radiation and convection are negligible by comparison and not included. The heat transfer coefficient, Eq. 2.9, and its uncertainty, Eq. 2.10, are shown below where δ_{RTD} is the uncertainty of the RTDs, 0.1 °C.

$$Q_{avg} = \frac{1}{5n}\sum_{i=1}^{5}\sum_{j=1}^{n}\dot{m}_i c_p\left(T_{exit_{ij}} - T_{inlet_{ij}}\right) \quad \textbf{Eq. 2.3}$$

$$\delta_{Q_{avg}} = \sqrt{\sum_{i=1}^{5} 2c_p\dot{m}_i{}^2\delta_{thermo}{}^2 + \delta_{\dot{m}}{}^2\left[\frac{1}{n}\sum_{j=1}^{n} c_p\left(T_{exit_{ij}} - T_{inlet_{ij}}\right)\right]^2} \quad \textbf{Eq. 2.4}$$

$$Q_{loss} = \frac{A_{loss}\left[T_{amb} - \left(\frac{T_{exit} + T_{inlet}}{2}\right)\right]}{\Omega} \quad \textbf{Eq. 2.5}$$

$$\delta_{Q_{loss}} = \sqrt{\left(\frac{T_{amb} - \left(\frac{T_{exit} + T_{inlet}}{2}\right)}{\Omega}\right)^2 \delta_A{}^2 + \left[\frac{A_{loss}\left(T_{amb} - \left(\frac{T_{exit}{}^2 + T_{inlet}{}^2}{2}\right)\right)}{\Omega}\right]^2 \delta_{thermo}{}^2} \quad \textbf{Eq. 2.6}$$

$$Q_{conv} = Q_{avg} - Q_{loss} \quad \textbf{Eq. 2.7}$$

$$\delta_{Q_{cond}} = \sqrt{\delta_{Q_{avg}}{}^2 - \delta_{Q_{loss}}{}^2} \quad \textbf{Eq. 2.8}$$

$$\bar{h} = \frac{Q_{cond}}{\left(T_{amb} - T_{plate}\right)A} \quad \textbf{Eq. 2.9}$$

$$\delta\bar{h} = \sqrt{\left[\frac{\delta_{Q_{cond}}}{A\left(T_{amb} - T_{plate}\right)}\right]^2 - \left[\frac{\delta_A Q_{cond}}{A^2\left(T_{amb} - T_{plate}\right)}\right]^2 + 2\delta_{RTD}{}^2\left[\frac{Q_{cond}}{A\left(T_{amb} - T_{plate}\right)^2}\right]^2} \quad \textbf{Eq. 2.10}$$

Where *i* is the summing variable for the number of measurements taken and *j* is the summing variable for the number of channels. T_{amb} is the ambient air temperature and T_{plate} is the temperature of the condensing surface.

Chapter 3 - Droplet Motion Results and Discussion

3.1 Definition of Droplet Modes[1]

Five different modes of droplet motion due to vibrations were of interest in simulations: rocking, ratcheting, ratcheting plus breakup, pumping, and ejection. A brief description of these modes follows, and simulation results are presented in subsequent sections. In the rocking mode, the contact line of the droplet does not slip; the droplet simply rocks back and forth without an average downward velocity. The ratcheting mode is similar to rocking in that the droplet rocks back and forth; however, this motion causes the contact line of the droplet to slip, and the droplet will have a downward velocity, while ratcheting back and forth [27, 28, 41, 42]. For ratcheting droplets with breakup, droplet motion is due to ratcheting but the parent droplet leaves behind a liquid trail that will spawn child droplets [43-45]. In pumping, the droplet flattens and elongated in sync with the periodic nature of the vibrations while the contact line remains pinned [42]. In the droplet ejection mode, vibrational forces are sufficiently large and the droplet elongates to a point where the surface tension forces can no longer maintain the droplet and a portion of the droplet breaks off from the surface [46, 47].

3.2 Droplet Motion Experiments[2]

Droplet motion tests were conducted at three different vibrational modes: 30 Hz and amplitude of ±0.1 mm, 60 Hz and amplitude of ±0.05 mm, and 100 Hz and amplitude of ±0.8 mm. These modes where selected by carefully visualizing droplets sprayed onto the surface from

---

[1] Section originally published in 40.Huber, R.A., et al., *Vibration-enhanced droplet motion modes: Simulations of rocking, ratcheting, ratcheting with breakup, and ejection.* Journal of Fluids Engineering, 2019. **141**(7).

[2] Figures and parts of section originally published in 38. Huber, R., et al. *Impacts of water quality on vibration-induced water droplet removal for cooling tower water capture*. in *ASTFE Digital Library*. 2019. Begel House Inc.

a squirt bottles reactions to different voltages supplied from the power generator that all had different results. Four different water qualities were tested as well with properties tabulated in Table 2.1. Three tests were run for each water quality and vibrational mode. The average droplet velocity was calculated by determining the distance between the top of our viewing area and the bottom of the viewing area and dividing by the time it takes a water droplet to cross the viewing area, or the total distance moved over the duration of the recording. Figure 3.1 Water droplet motion of a) DI b) Salt c) CTB d) FGD at a frequency of 30 HZ and an amplitude of ±0.1mm [38] shows the droplet motion for a) DI b) salt c) CTB d) FGD at the 30 Hz case over 1.1 seconds. The DI droplet moves the farthest while the salt droplet moves the shortest distance over a given period.

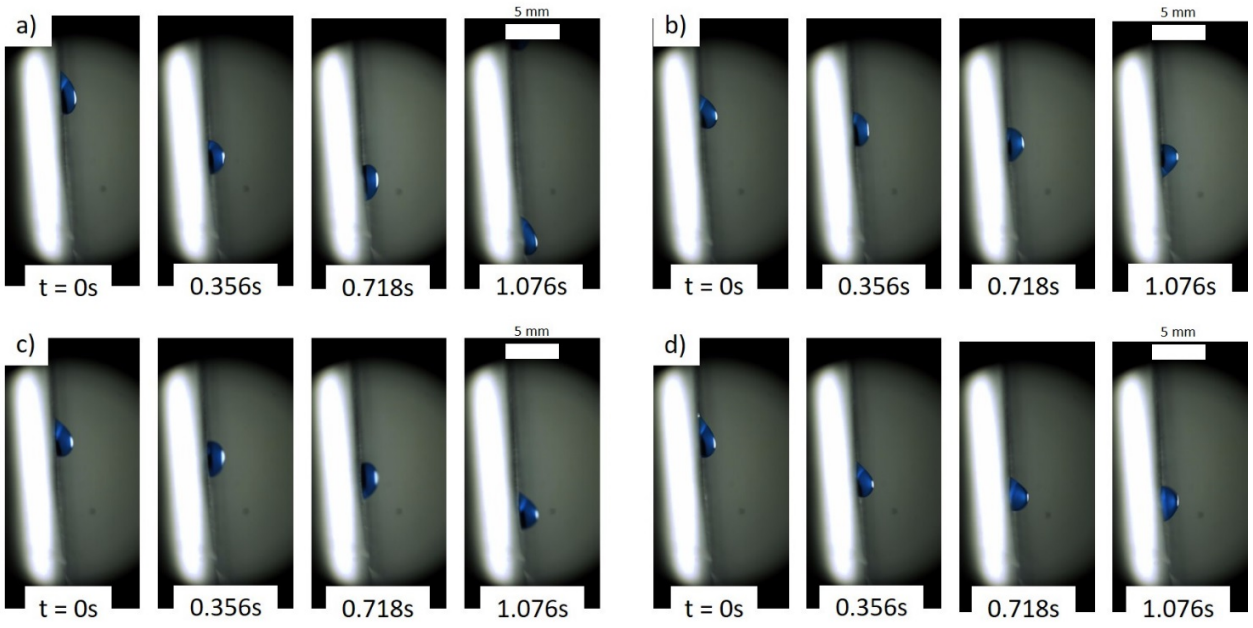

Figure 3.1 Water droplet motion of a) DI b) Salt c) CTB d) FGD at a frequency of 30 HZ and an amplitude of ±0.1mm [38]

Figure 3.2 Water droplet motion of DI at a frequency of 60 HZ and an amplitude of ±0.05mm [38] shows the droplet motion for DI water at the 60 Hz test case over 6.5 seconds. The droplet barely moves for this test case resulting in low velocities (~0.7 mm/s) and the same is true across

all the water qualities. This is likely due to wave interference in the water droplet producing a resultant wave with a smaller amplitude. The lower amplitude does not provide enough force to incite droplet motion.

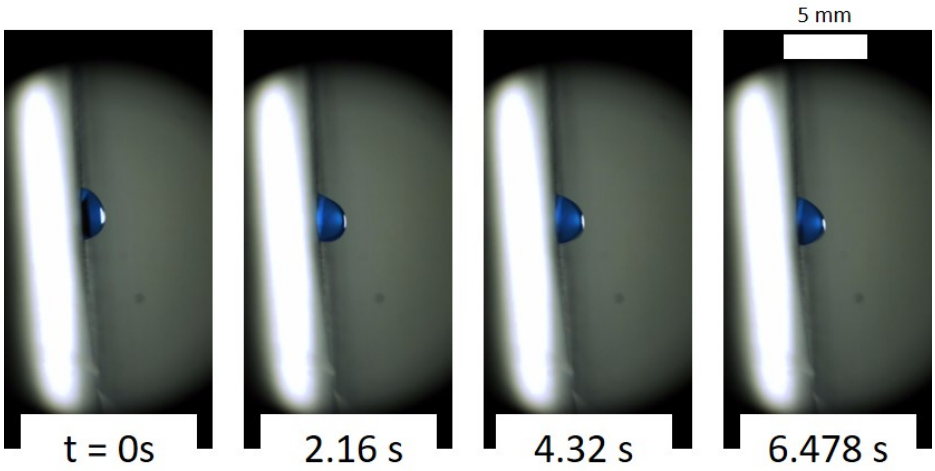

Figure 3.2 Water droplet motion of DI at a frequency of 60 HZ and an amplitude of ±0.05mm [38]

Figure 3.3 Water droplet motion of a) DI b) Salt c) CTB d) FGD at a frequency of 100 HZ and ±0.8mm amplitude [38] shows the droplet motion for a) DI b) Salt c) CTB d) FGD at the 100 Hz test case over 0.3 seconds. Once again, this DI droplet moves the farthest, but this time this CTB droplet moves the least. Not shown in the figure is that all of the water qualities had some droplets that ejected off the surface. This was not studied further due to the difficulty of capturing an ejecting droplet on camera.

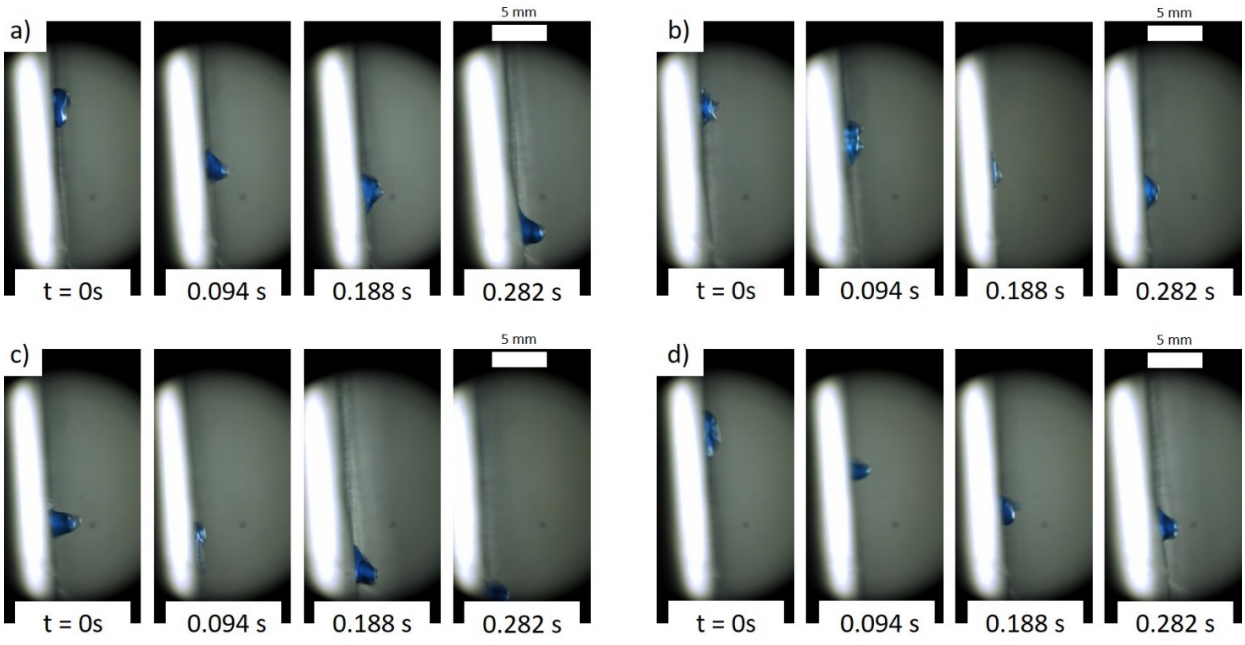

Figure 3.3 Water droplet motion of a) DI b) Salt c) CTB d) FGD at a frequency of 100 HZ and ±0.8mm amplitude [38]

3.2.1 Water Quality Property Impacts

Figure 3.4 Velocities of different water quality droplets at a frequency of 30 HZ and an amplitude of ±0.1mm versus a) viscosity b) surface tension [38]Figure 3.4a shows the velocities of droplets for each different water quality at 30 Hz versus viscosity; an inversely proportional trend is observed. Since the force applied to each of the droplets is about the same, the increasing viscous forces would hinder the droplet motion and slow the droplets' sliding. Figure 3.4b shows the velocities of each different water quality droplet at 30 Hz versus surface tension and a proportional trend can be seen, likely due to the effects that surface tension has on hydrophobicity. The higher the surface tension of a fluid is the more it will want to stick to itself than a surface. Since all the waters were tested on the same surface, the increase in surface tension would decrease the contact area the droplet has with the surface, this would lead to a decrease in pinning forces resulting in more force being able to go towards droplet acceleration.

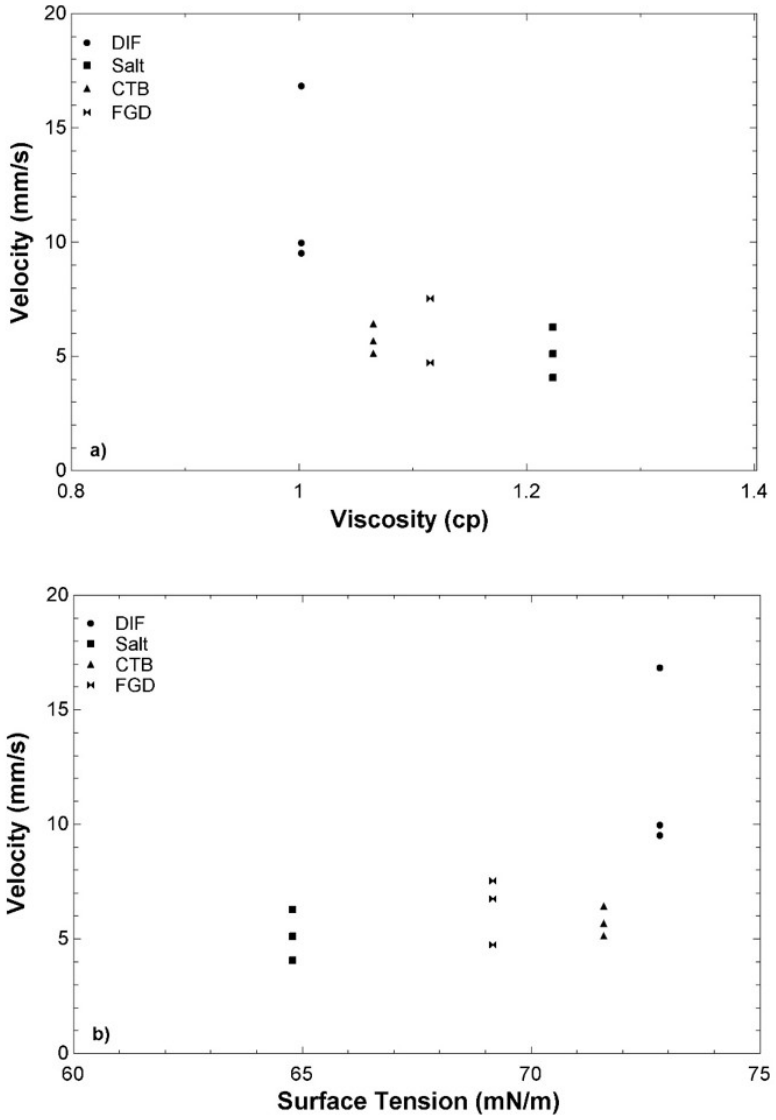

Figure 3.4 Velocities of different water quality droplets at a frequency of 30 HZ and an amplitude of ±0.1mm versus a) viscosity b) surface tension [38]

Figure 3.5 show the velocities of three tests for each different water quality at 60 Hz versus a) viscosity and b) surface tension. At first glance, the trends observed for viscosity and surface tension appear to be reversed from the trends observed in Figure 3.4. However, the differences in velocity are minimal and the velocities are roughly constant. Figure 3.6 show the velocities of three tests for each different water quality at 100 Hz versus a) viscosity and b) surface tension. The same trends observed in Figure 3.4 are present in this graph as well.

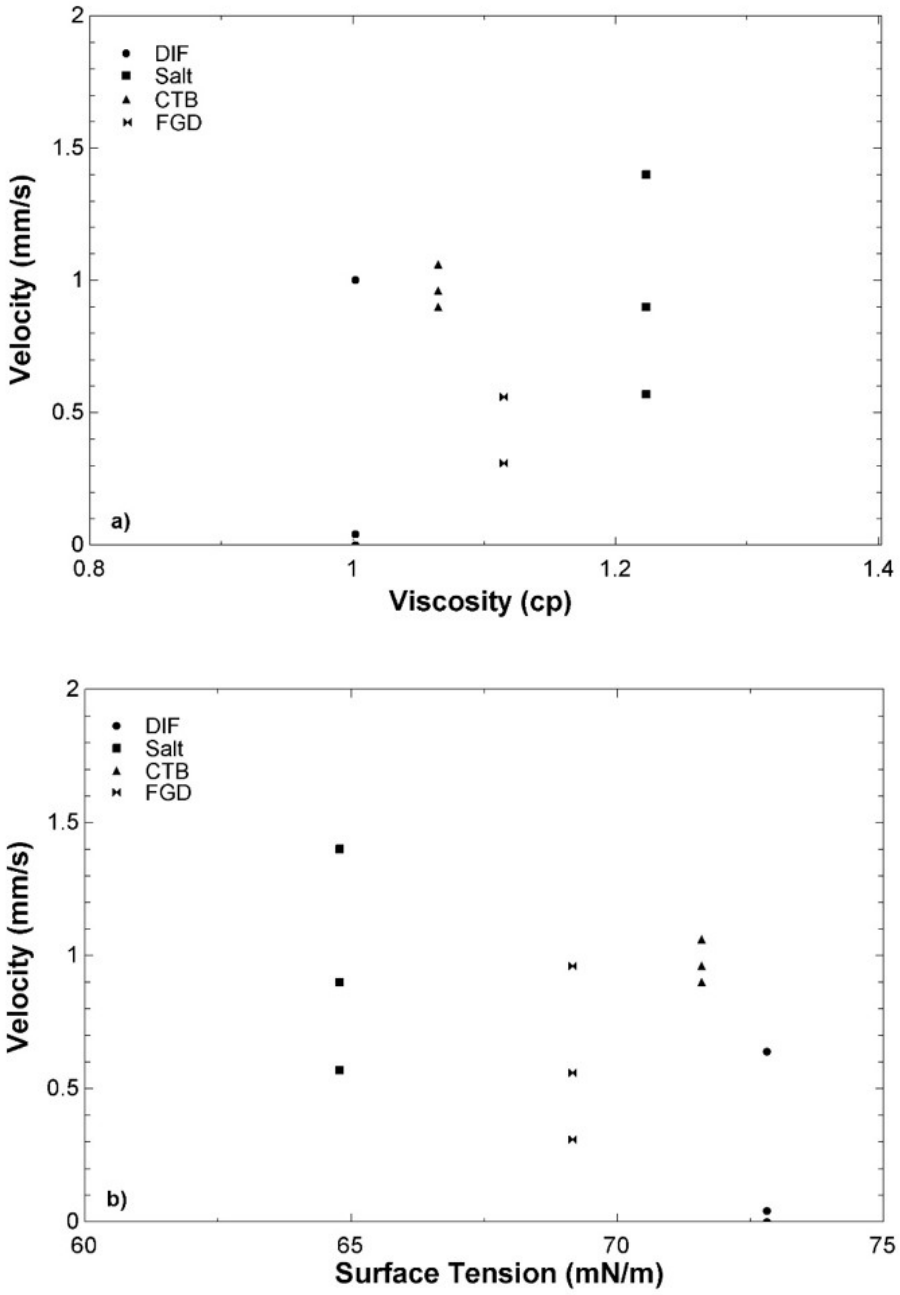

Figure 3.5 Velocities of different water quality droplets at a frequency of 60 HZ and an amplitude of ±0.05mm versus a) viscosity b) surface tension [38]

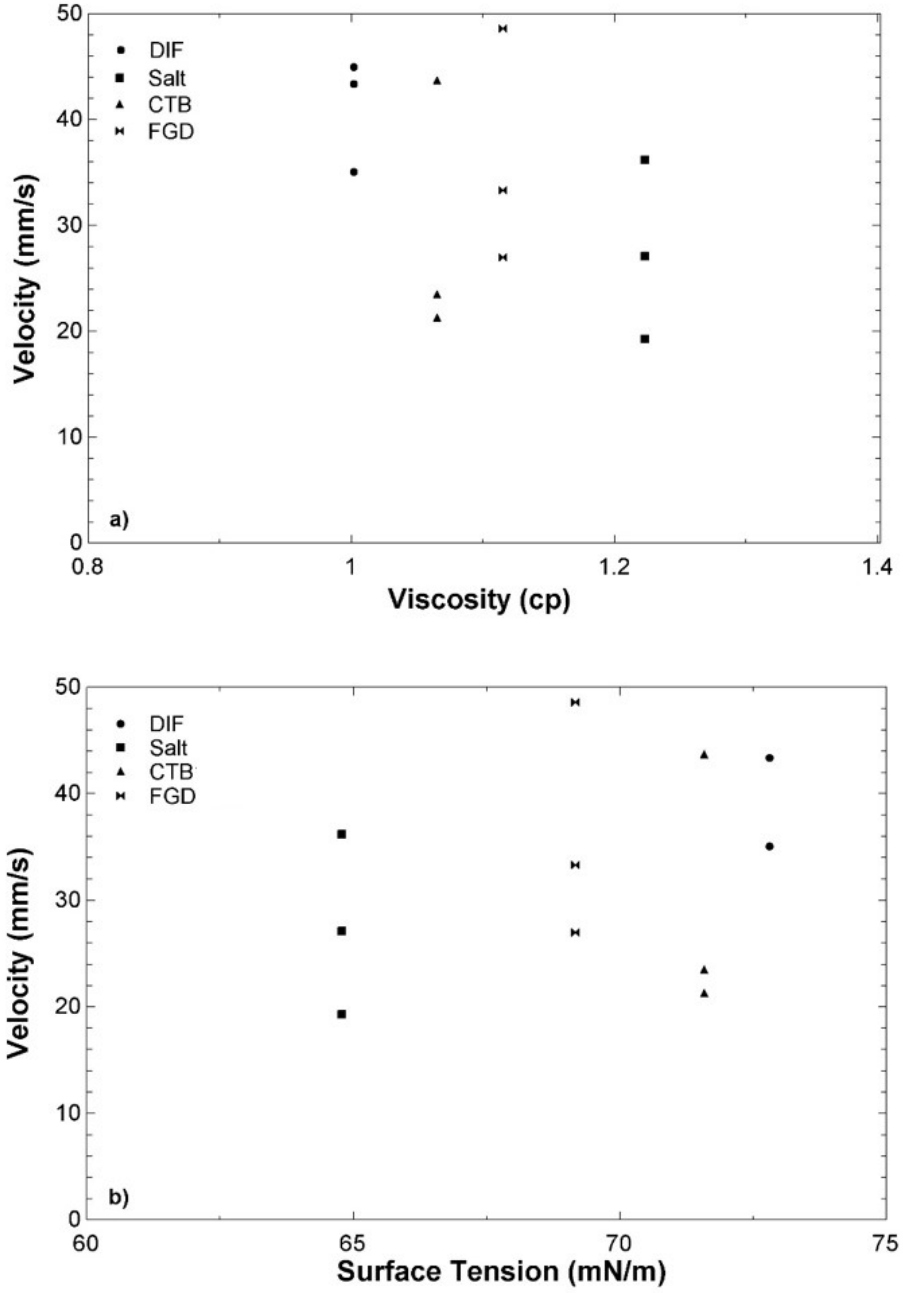

Figure 3.6 Velocities of different water quality droplets at a frequency of 100 HZ and an amplitude of ±0.8mm [38]

Chapter 4 - Droplet Motion Simulations[3]

4.1 Simulation Software

Due to the complex, transient nature of droplet motion under vibrations, multiple software packages were evaluated (FLUENT, Flow3D, and XFlow). Finite volume method CFD software (e.g FLUENT and Flow3D) was not able to allow for contact angle hysteresis settings and struggled with modeling the three-phase contact of the droplet and was, therefore, not selected. CFD solutions utilizing the lattice Boltzmann method (LBM) can handle these challenges with moving contact lines. The LBM is an emerging tool in CFD applications due to inherent advantages of the method, including:

- Well-posed and accurate handling of multi-phase and multi-component flows.
- Complex boundaries are handled easily.
- Simulations can be parallelized efficiently allowing the use of fine resolution, small timesteps and advanced turbulence models (LES) [48].

Xflow, an LBM software, was selected after comparing simulations to experiments. It was able to account for advancing and receding contact angles as well as properly modeling a moving contact line.

4.1.1 XFlow Methodology

XFlow solves the discretized Boltzmann equation and collision models to simulate Newtonian and non-Newtonian fluid flows. Previous researchers have used lattice Boltzmann

[3] Sections of this chapter and all figures, tables, and equations were first published in 40. Huber, R.A., et al., *Vibration-enhanced droplet motion modes: Simulations of rocking, ratcheting, ratcheting with breakup, and ejection.* Journal of Fluids Engineering, 2019. **141**(7).

methods to successfully simulated a range of flow conditions, including porous media, human blood flow, vortex shedding, multi-phase flows, and droplet dynamics [49-54].

4.1.1.1 Lattice Structure

The lattice structure of LBM works by discretizing a Cartesian space into a set number of discrete points with a discrete set of velocity directions. The different lattice structures use the naming scheme DnQm, where *n* is the dimension of a problem and *m* represents the number of discrete velocity directions, including no velocity. For three-dimensional cases, XFlow uses the D3Q27 lattice scheme, which XFlow organizes in an octree structure. The use of this lattice scheme provides a fourth-order spatial discretization in return for higher computational cost [55].

4.1.1.2 Geometric Modeling

XFlow uses the Wall-Adapting Local Eddy (WALE) viscosity model of LES to model turbulence. This provides a consistent local eddy-viscosity and near wall behavior. In the LBM, the strain rate tensor is locally available, which allows for efficient implantation of LES models. In addition to the WALE model XFlow also uses wall functions in order to model the boundary layer, the Wall-Modeled LES approach (WMLES) [55]. A generalized law of wall given by Shih et al. [56] models the boundary layer. To discretize the geometry XFlow projects a set of discrete velocities onto the geometry tessellation. Since each lattice node can detect up to 27 geometry projections, a high level of detail is provided for the geometry discretization. The flexibility of the octree structure and the WMLES allows XFlow to address fluid-structure interactions, thereby modeling dynamic geometries, such as the vibrating surface in this work. The WALE and WMLES models are used in the modeling of the solid-fluid interaction, which is a primary factor in modeling droplet motion. To create a dynamic geometry the geometries' position was enforced based on user-defined position equations. To accomplish this, XFlow updates the lattice

structure every time step to mark lattice nodes as either fluid or solid. The discrete velocities are projected every time step as well to determine the new distance to the wall. The boundary conditions in XFlow are resolved using the bounce-back method, in which the incoming PDFs at the wall node are reflected back to the fluid node [55].

4.1.1.3 Fluid Modeling

XFlow utilizes the Boltzmann transport equation in the continuum space with discrete velocities,

$$\frac{\partial F_i}{\partial t} + e_i \cdot \nabla F_i = \Omega_i \quad i = 1, \dots, b \qquad \textbf{Eq. 4.1}$$

where F_i are the probability distribution functions, e_i are the velocity vectors and Ω_i are the collision operators. XFlow's collision operator is implemented in central momentum space. The raw moments are defined as,

$$\tilde{\mu}_{x^k y^l z^m} = \sum_i^N F_i (e_{ix} - u_x)^k \left(e_{iy} - u_y\right)^l (e_{iz} - u_z)^m \qquad \textbf{Eq. 4.2}$$

where u is the macroscopic velocity vector, μ is the raw moment, and k, l, and m are the orders of moments taken in x, y, and z directions respectively. XFlow's collision operator is based on a multiple relaxation time scheme shown in Eq. 4.3,

$$\Omega_i^{MRT} = -M_{ij}^{-1} \hat{S}_{ij} \left(\mu_i^{eq} - \mu_i\right) \qquad \textbf{Eq. 4.3}$$

where M is the transformation matrix, $\hat{S}$ is the diagonal relaxation matrix, and μ^{eq} is the raw moment at equilibrium. XFlow uses the Chapman-Enskog expansion to identify the kinematic viscosity, υ, with the relaxation time, τ, and speed of sound, c_s, as seen in Eq. 4.4.

$$\upsilon = c_s^2 \left(\tau - \frac{1}{2}\right) \qquad \textbf{Eq. 4.4}$$

The use of the Chapman-Enskog expansion demonstrates that the LBM is second-order accurate in space [55].

4.2 Simulation Set-up and Validation

A rectangular domain of 1.5 mm in the *x*-direction, 5 mm to 62 mm in the *y*-direction, and 3 mm in the *z*-direction was created, and gravity was applied in the *y*-direction. A 2.6-mm diameter hemispherical water droplet was initialized in air on the vertical hydrophobic wall centered at (0,0,0), with the volume remaining constant throughout the simulation. Water and air properties were based on 20 °C and atmospheric pressure. Sinusoidal position functions were used to simulate a vibrating surface (Eq. 4.5 and Eq. 4.6), resulting in the following acceleration functions (Eq. 4.7 and Eq. 4.8),

$$x = A\cos(2\pi f t) \quad \textbf{Eq. 4.5}$$

$$y = -B\cos(2\pi f t) \quad \textbf{Eq. 4.6}$$

$$\ddot{x} = 4\pi^2 f^2 B\cos(2\pi f t) \quad \textbf{Eq. 4.7}$$

$$\ddot{y} = 4\pi^2 f^2 B\cos(2\pi f t) \quad \textbf{Eq. 4.8}$$

$$S_v = u\frac{\Delta t}{\delta} < .1 \quad \textbf{Eq. 4.9}$$

where *A* is the *x*-amplitude, *B* is the *y*-amplitude, *f* is frequency, and *t* is time; the *x*-axis is perpendicular to the vertical wall and the *y*-axis is parallel to the vertical wall. Maximum accelerations were calculated by setting the cosine term to one in the acceleration functions. *X* & *y*-direction vibrations simulations were conducted to experimentally validate simulations while *y* only direction simulations were done to determine the impacts on droplet motion. Simulation times were generally for three full periods of motion unless there was significant computational time (i.e., simulations required multiple days even when conducted on 28 parallel cores) needed

to accomplish this. The time step for the simulation was determined by Eq. 4.9 where u was 1 m/s, 5 m/s, or 10 m/s if the average downward velocity of the drop was greater than 1 m/s. Where S_v is defined as a stability parameter used to determine if the simulation satisfies the Courant-Friedrichs-Lewy condition, u is the maximum velocity, Δt is the time step, and δ is the resolved scale. To allow for a contact angle hysteresis, the advancing (120°) and receding (60°) contact angles were assigned independently based on experimental data of a 2.6 mm diameter drop moving down a vertical Teflon surface. Table 4.1 shows the simulation matrix and the time steps used.

Table 4.1Simulation parameters, including a) y-amplitude [mm] b) Time step [s] c) Total lattice time d) Total lattice distance traveled e) Average downward lattice velocity for different test cases [39]

Frequency (Hz)	a) *Y*-amplitude [mm] b) Time step [s] c) Total lattice time d) Total lattice distance traveled e) Average downward lattice velocity						
10	a	±0.05	±0.5	±1.8	±5	±15	±50
	b	5.0E-06	5.0E-06	5.0E-06	5.0E-06	5.0E-06	5.0E-06
	c	60000	60000	60000	27545	27600	10000
	d	0	0	10	170	560	1160
	e	0.0000	0.0000	0.0002	0.0062	0.0203	0.1160
30	a	±0.05	±0.02		±1.67	±5	±5.56
	b	5.0E-06	5.0E-06		5.0E-06	2.5E-05	2.5E-05
	c	20000	20000	-	15800	34400	20800
	d	0	26		160	560	560
	e	0.0000	0.0013		0.0101	0.0163	0.0269
70	a	±0.037	±0.05	±0.306	±0.5	±1.02	±5
	b	5.0E-06	5.0E-06	5.0E-06	5.0E-06	5.0E-06	2.5E-05
	c	10000	10000	10000	10000	7600	20000
	d	2	4	60	100	170	860
	e	0.0002	0.0004	0.0060	0.0100	0.0224	0.0430
100	a	±0.018	±0.05	±0.15	±0.5	±5	
	b	5.0E-06	5.0E-06	5.0E-06	5.0E-07	5.0E-07	
	c	6000	6000	2000	20000	13400	-
	d	1	4	10	50	480	
	e	0.0002	0.0007	0.0050	0.0025	0.0358	

4.2.2 Grid Independence Study

Grid independence was determined by determining the kinetic energy of the drop versus the number of lattice points to ensure the resolution did not affect the outcome. Figure 4.1 shows the kinetic energy of the water drop over time for five different resolved scales, D/N, where D was defined as the initial water droplet diameter of 2.6 mm and N equaled 30, 40, 50, 75, and 100 elements across the diameter. $D/50$ was selected to balance the tradeoffs between minimizing simulation time and ensuring accurate simulations.

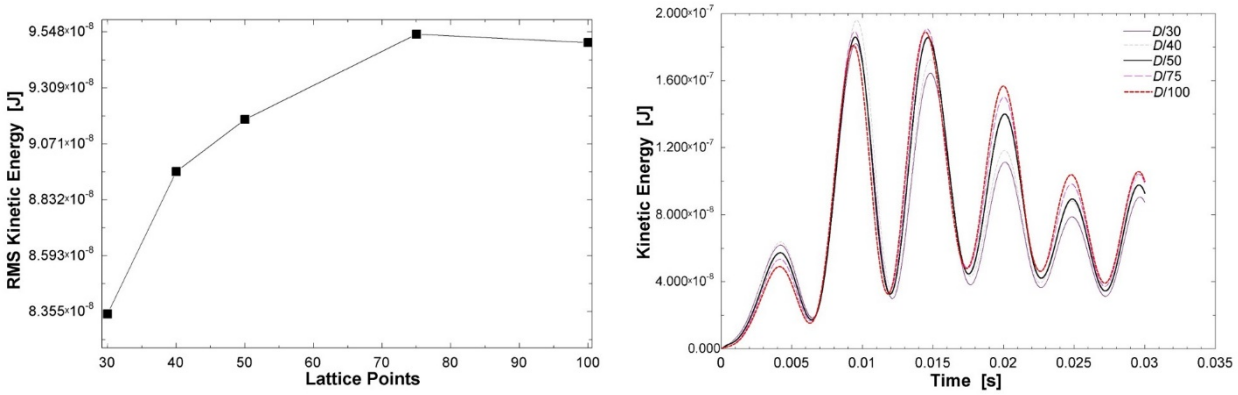

Figure 4.1 Grid independence study using kinetic energy, (left) root mean square kinetic energy over 0.03 seconds and (right) kinetic energy with time [40]

4.2.3 Experimental Validation

For validation purposes, simulations were conducted for two experimental droplet motion cases from chapter 3. In the first experimental case, the vibrational frequency was 30 Hz, and the x and y amplitudes were ± 0.1 mm (i.e., x maximum acceleration of 3.55 m/s^2) and ± 0.2 mm (i.e., y maximum acceleration of 7.11 m/s^2), respectively. Figure 4.2 shows the results from the experiments and the simulation with the same conditions.

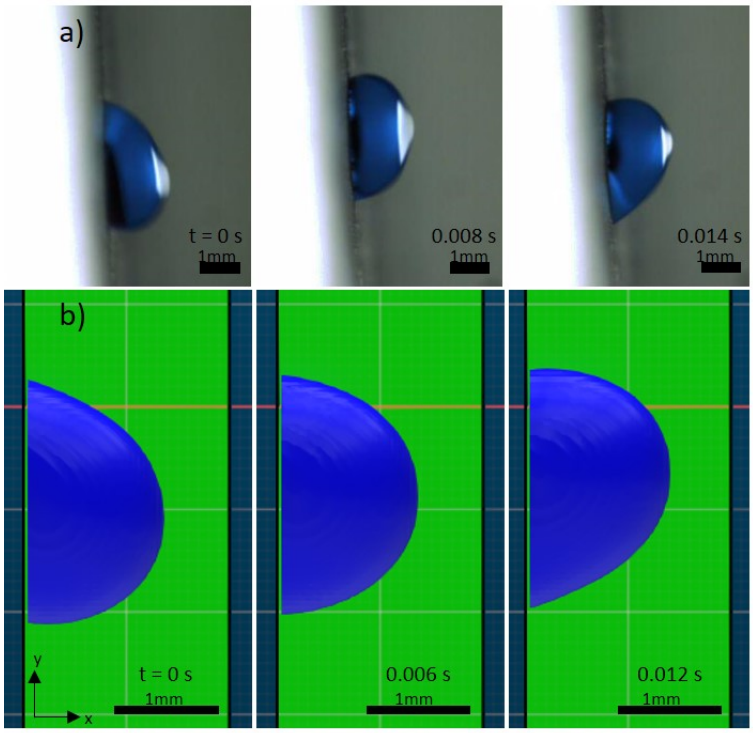

Figure 4.2 Droplet motion of a) an experimental droplet and b) simulated droplet at 30 Hz, x-amplitude ±0.1 mm, y-amplitude ±0.2 mm [40]

Average downward velocities for the experimental droplet was 16 ± 0.14 mm/s and the simulation's average downward velocity was 15 mm/s. From the velocity and visual similarities it was determined that the motion of ratcheting droplets is being properly captured by the software. A second simulation was conducted to determine if the software could accurately capture the physics of droplet ejection. For this case, a frequency of 100 Hz was selected for simulations and experiments with *x*- and *y*-amplitudes of ± 0.4 mm (i.e., *x* maximum acceleration of 158 m/s^2) and ± 0.15 mm (i.e., *y* maximum acceleration of 59 m/s^2), respectively; the results can be seen in Figure 4.3. The visual similarities and the close average downward velocities (i.e., 41 ± 0.45 mm/s and 40 mm/s for the experimental and simulated velocities respectively) shows that the ejection of water droplets can be properly modeled as well. Xflow demonstrated that it could model both ratcheting and ejecting droplets under vibrations.

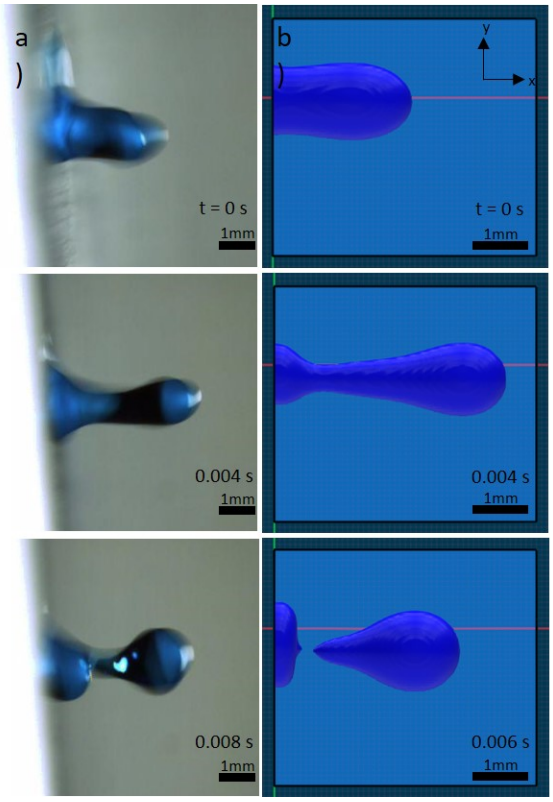

Figure 4.3 Droplet motion for a) an experimental droplet and b) simulated droplet at 100 Hz, x-amplitude ±0.4 mm, y-amplitude ±0.15 mm [40]

4.3 Simulation Results and Discussion

Two main studies were conducted using simulations. One was the effect of vibration direction, including the impacts that vibrations in the direction perpendicular and parallel to the surface have versus only parallel to the surface. This was useful since it is easier to uncouple the vibrations in simulations compared to experiments. The other investigation was the impacts that acceleration has on the droplet motion.

4.3.1 Impacts of Vibrational Direction

The main point of this study is to determine if the vibrations in the x-direction aid in the shedding of droplets or are just a waste of energy. Simulations with the same y-direction

frequencies and amplitudes as the validation cases were compared. Figure 4.4 shows the droplet under x and y vibrations in (a) and only y in (b) for the 30 Hz case.

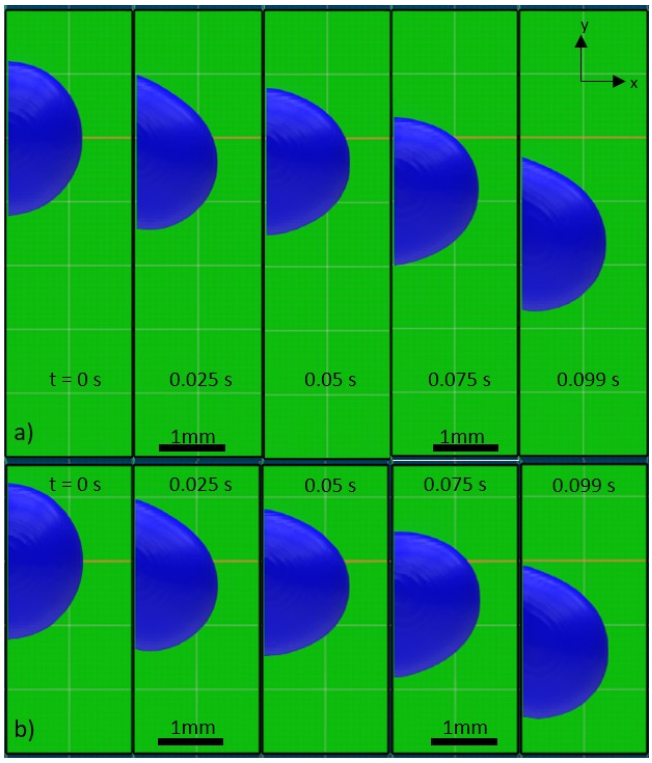

Figure 4.4 30 Hz simulated droplet motion for a) x- and y-vibrational forces and b) only y-vibrational forces (x-amplitude ±0.1 mm, y-amplitude ±0.2 mm) [40]

The droplets both ratchet down the surface in the direction of gravity. The droplet experiencing y-only vibrations experiences a slightly slower average downward velocity of 11 mm/s compared to the 15 mm/s of droplet experiencing vibrations in x and y-direction. The droplet experiencing vibrations in both directions flattens slightly (0.05 mm) compared to the droplet not experiencing x-direction vibrations.

For the 100 Hz vibrational case, the simulations resulted in two different droplet modes. The droplet experiencing vibrational forces in two directions moved at an average velocity of 40 mm/s and ejected from the surface, as seen in Figure 4.5a. However, the droplet only

experiencing y-directional vibrations did not eject and only ratcheted down the surface at a speed of 60 mm/s, as seen in Figure 4.5b.

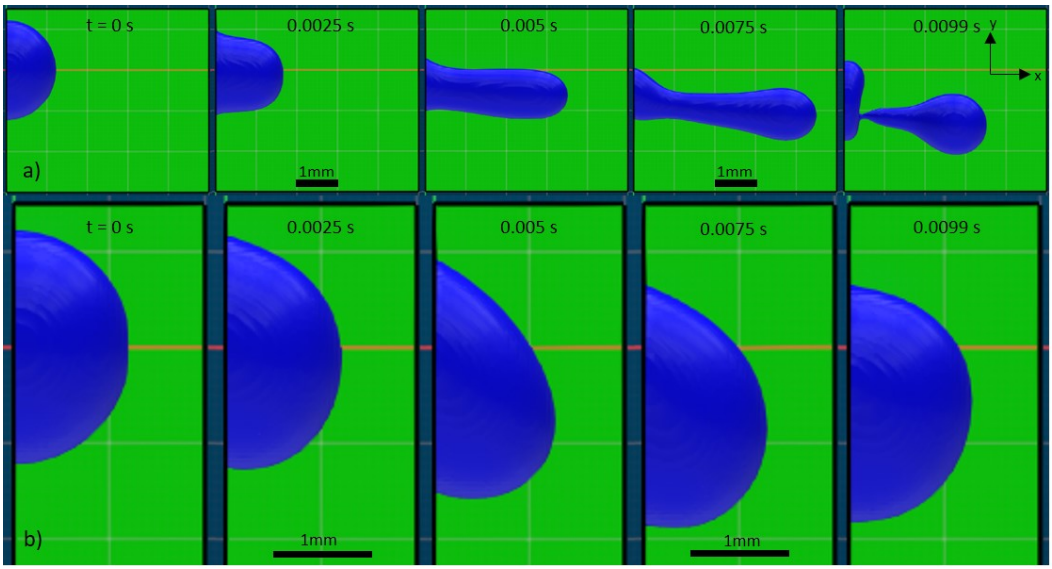

Figure 4.5 100 Hz simulated droplet motion for a) x- and y-vibrational forces b) only y-vibrational forces (x-amplitude ±0.4 mm, y-amplitude ±0.15 mm) [40]

While the difference in average downward velocity is still not significant, the droplet not ejecting from the surface allows for departing droplets to sweep away smaller droplets below them as mentioned in chapter 1. Due to this, the subsequent simulation research will focus on the y-only vibrations.

4.3.2 Impact of Acceleration

Three maximum accelerations were tested for each frequency (i.e., 7.11 m/s^2, 59.2 m/s^2, and 197 m/s^2). The other three tests used the same amplitudes across the frequencies; all tests are shown in Table 4.2.

Table 4.2 Test matrix of simulation frequencies, amplitudes, and max accelerations [39]

Frequency (Hz)	y-amplitude (mm) [Maximum y-acceleration (m/s^2)]					
10	±0.05 [0.197]	±0.5 [1.97]	±1.8 [7.11]	±5 [19.7]	±15 [59.2]	±50 [197]
30	±0.05 [1.78]	±0.02 [7.11]	-	±1.67 [59.2]	±5 [178]	±5.56 [197]
70	±0.037 [7.11]	±0.05 [9.67]	±0.306 [59.2]	±0.5 [96.7]	±1.02 [197]	±5 [967]
100	±0.018 [7.11]	±0.05 [19.7]	±0.15 [59.2]	±0.5 [197]	±5 [1970]	-

Figure 4.6a shows the average downward velocities of the simulations run with a frequency of 10 Hz over a range of maximum accelerations, 7.11 m/s^2, 0.197 m/s^2, and 59.2 m/s^2, in Figure 4.6b, c, and d, respectively. As expected, the larger the maximum acceleration is, the faster the water droplet moves. However, there are two cases for the 10 Hz vibrations that do not produce any downward velocity (i.e., 0.197 m/s^2, seen in Figure 4.6c, and 1.97 m/s^2, not pictured); these two rocking motions are shown as red triangles on the graph in Figure 4.6a. In these cases, the vibrations are strong enough to shake the droplet slightly but not strong enough to overcome the pinning forces on the surface.

Generating large maximum accelerations at low frequencies requires very large vibrational amplitudes. In Eq. 4.8, the frequency term is squared whereas the amplitude term is proportional. To create large maximum accelerations at low amplitudes, the vibrational frequency was raised. Figure 4.7a show the average downward velocities from the 30 Hz simulations at a range of maximum accelerations: 59.2 m/s^2, 7.11 m/s^2, and 178 m/s^2 in Figure 4.7b, c, and d, respectively. Similarly, the average downward velocity of the drop increased with increasing maximum acceleration. There is also one maximum acceleration that was only able to induce rocking motion in the droplet (i.e., 1.78 m/s^2). The maximum acceleration for the rocking droplet at 30 Hz was close to a rocking droplet case at 10 Hz, 1.78 m/s^2 and 1.98 m/s^2 respectively. For both tests, the smallest maximum acceleration tested that produced an average

downward velocity was 7.11 m/s^2. In Figure 4.7d at a maximum acceleration of 178 m/s^2, this droplet exhibits the ratcheting breakup mode mentioned in chapter 3. A child droplet is spawned from the ratcheting parent droplet.

The average downward velocities over a range of maximum accelerations for 70 Hz (Figure 4.8a), while Figure 4.8b, c, and d show images from the 197 m/s^2, 59.2 m/s^2, and 9.67 m/s^2 maximum acceleration cases, respectively. Similarly, Figure 4.9a shows the average downward velocities over a range of maximum accelerations for 100 Hz, while Figure 4.9b, c, and d show images from the 197 m/s^2, 59.2 m/s^2, and 7.11 m/s^2 cases, respectively. The lowest tested maximum acceleration for both of these frequencies was 7.11 m/s^2, and, similarly to the 10 Hz and 30 Hz cases, these droplets experienced ratcheting motion. However, all of these droplet velocities are very low; therefore, the results suggest that the transition from rocking motion to ratcheting motion is a function of maximum acceleration for droplets of the same mass (i.e., 7.11 m/s^2 for this case).

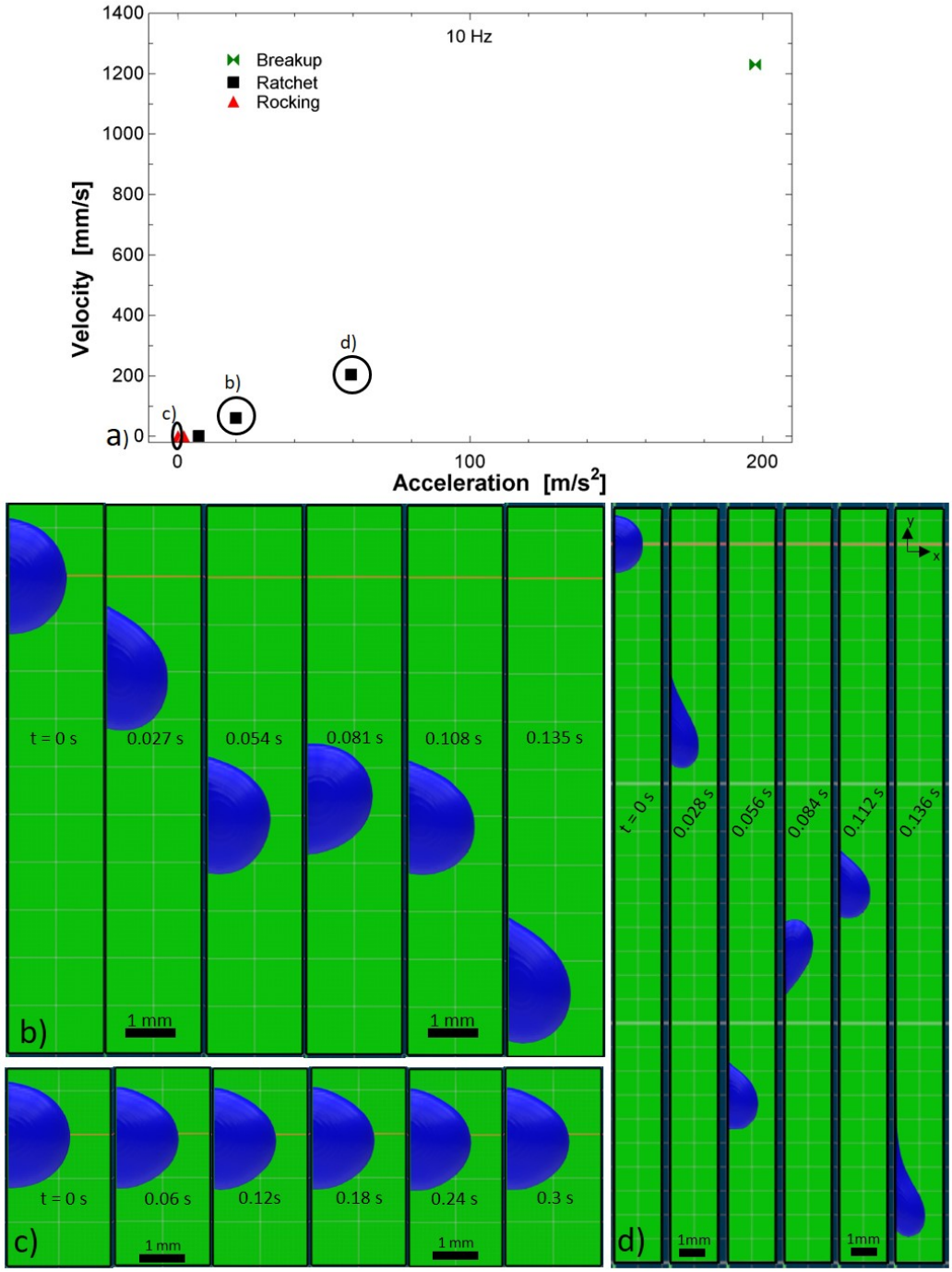

Figure 4.6 10 Hz simulated droplet a) velocities for given accelerations and simulations with applied accelerations of b) 7.11 m/s^2, c) 0.197 m/s^2, and d) 59.2 m/s^2 images [40]

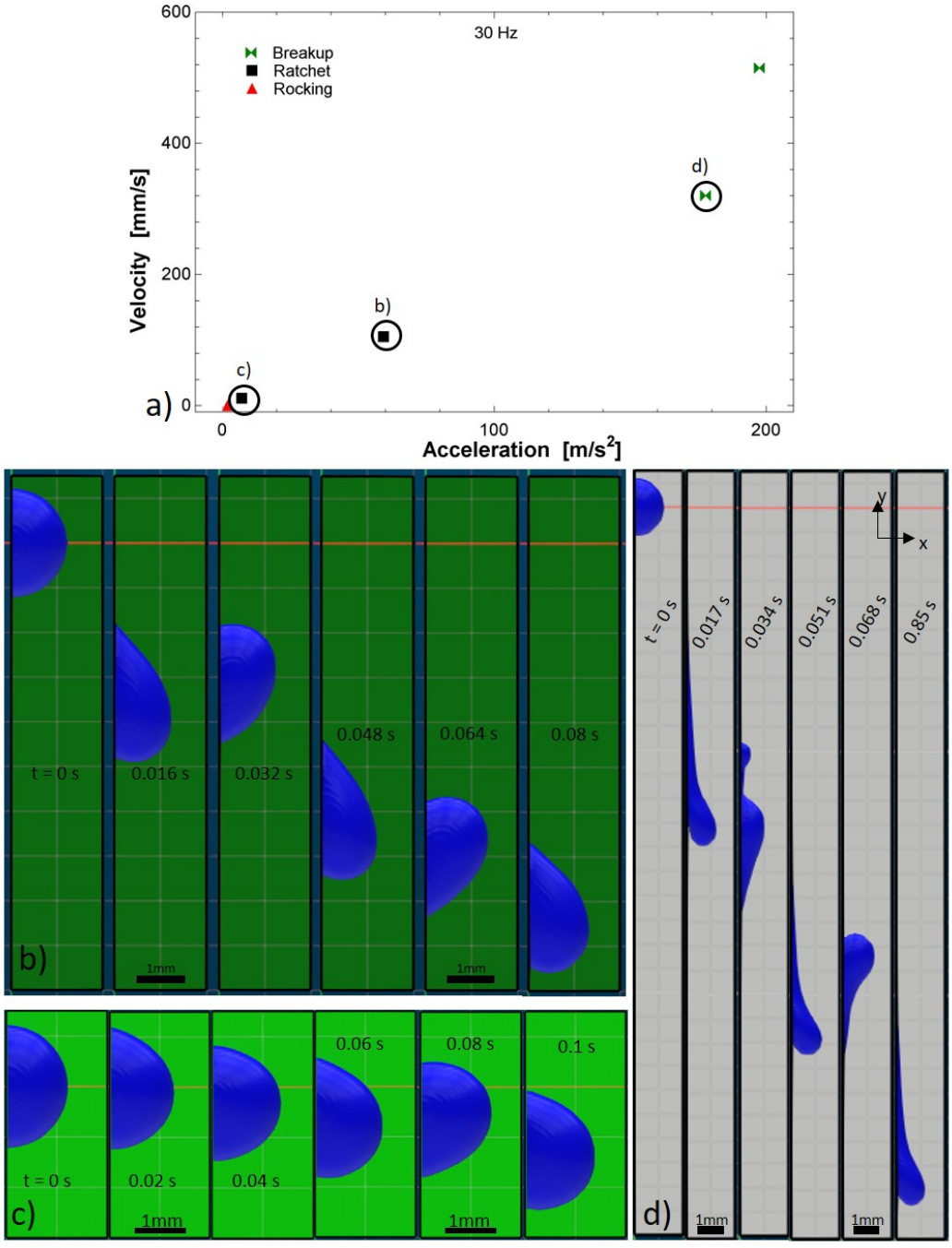

Figure 4.7 30 Hz simulated droplet a) velocities for given accelerations b) 59.2 m/s^2, c) 7.11 m/s^2, and d) 178 m/s2 [40]

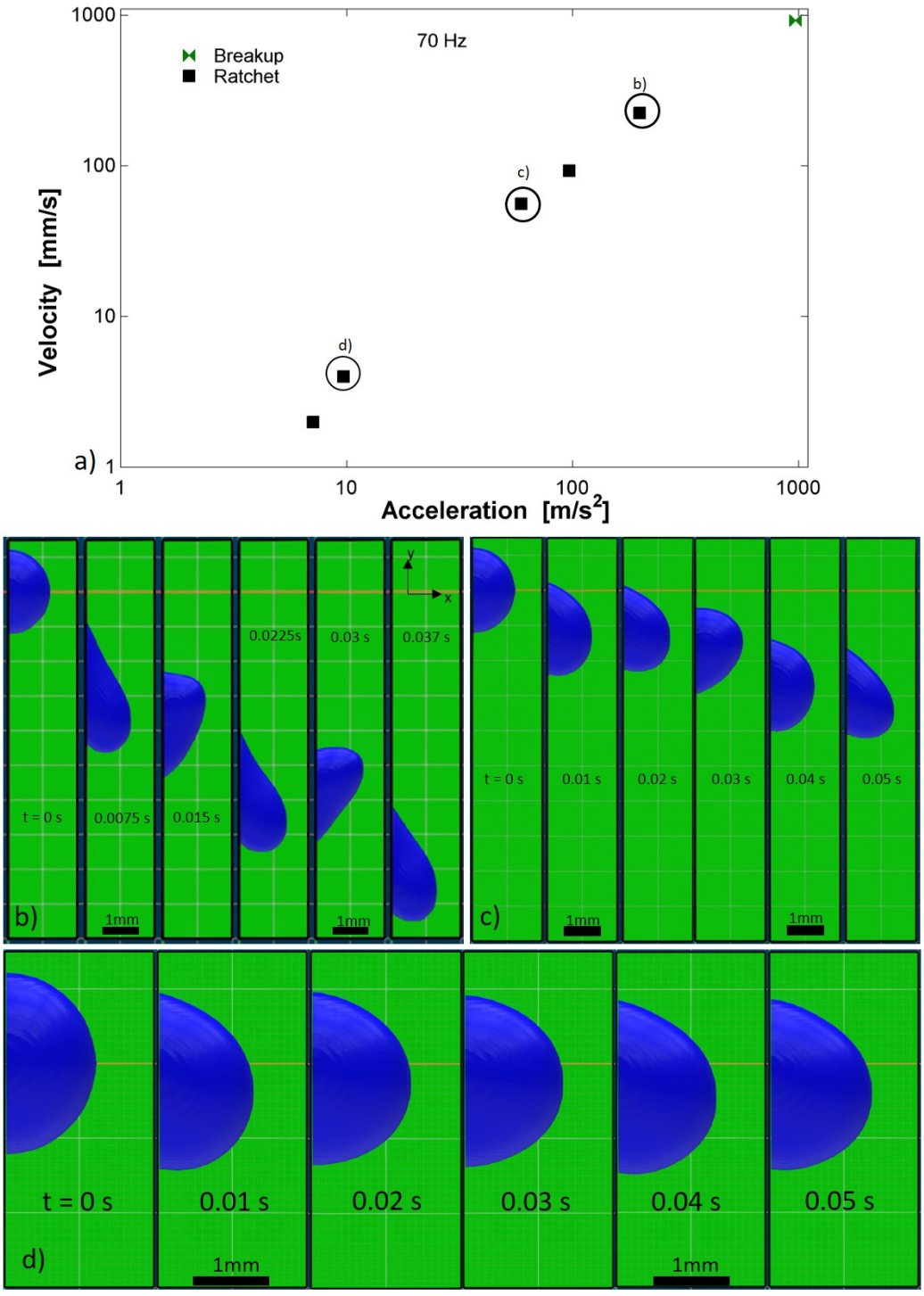

Figure 4.8 70 Hz simulated droplet a) velocities for given accelerations b) 197 m/s^2 images c) 59.2 m/s^2 images d) 9.67 m/s^2 images [40]

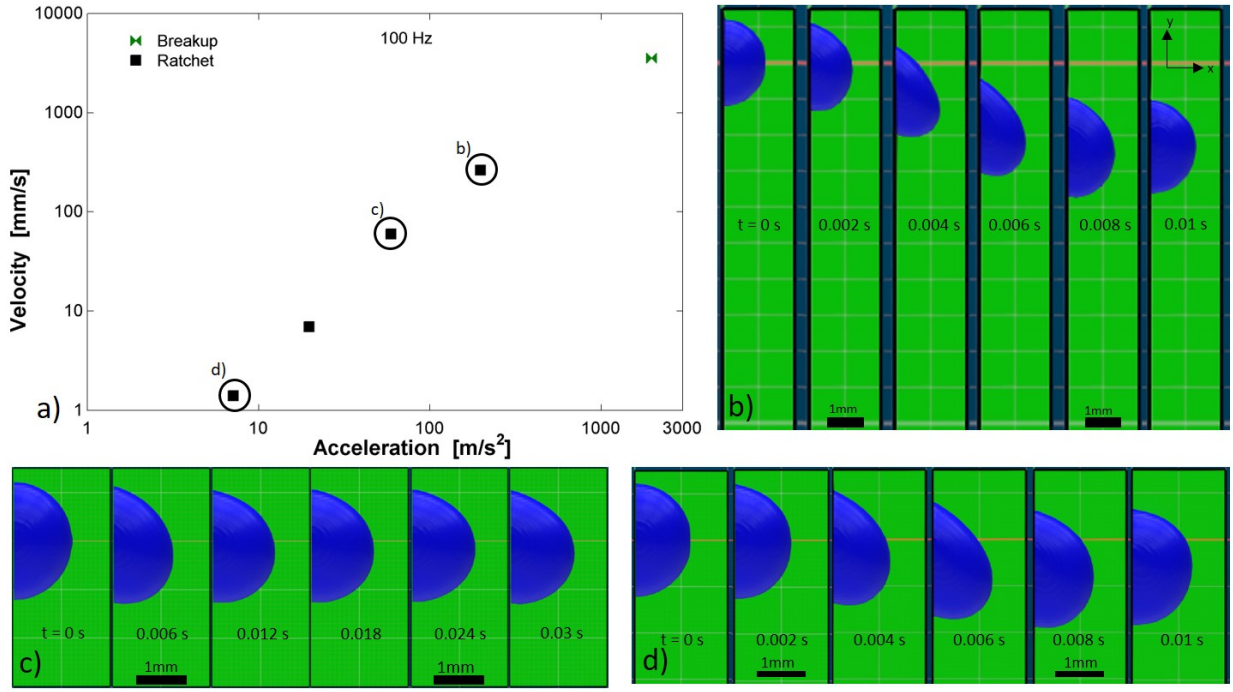

Figure 4.9 100 Hz simulated droplet a) velocities for given accelerations b) 197 m/s^2 images c) 59.2 m/s^2 images d) 7.11m/s^2 images [40]

To determine if the velocity of a droplet is a function of maximum acceleration only, the average downward velocities for the three set maximum accelerations were compared across all frequencies, seen in Figure 4.10. There is a trend in the 59.2 m/s^2 and 197 m/s^2 maximum accelerations that the average downward velocity will decrease as the frequency is increased from 10 Hz to 70 Hz and the 100 Hz case is close to the 70 Hz case. However, for the maximum acceleration of 7.11 m/s^2, the trend is unclear and the 30 Hz case has the highest average downward velocity; it is likely this may be due to the predicted resonant frequency of a 2.6-mm water droplet is 40 Hz. Eq. 4.10 shows the calculation for resonance frequency proposed by Perez et al. [57],

$$f_r = \sqrt{\frac{4}{5}\frac{\sigma}{\pi\rho V}} \qquad \textbf{Eq. 4.10}$$

where f_r is the resonance frequency, σ is the surface tension of water, ρ is the density of water, and V is the volume of the droplet.

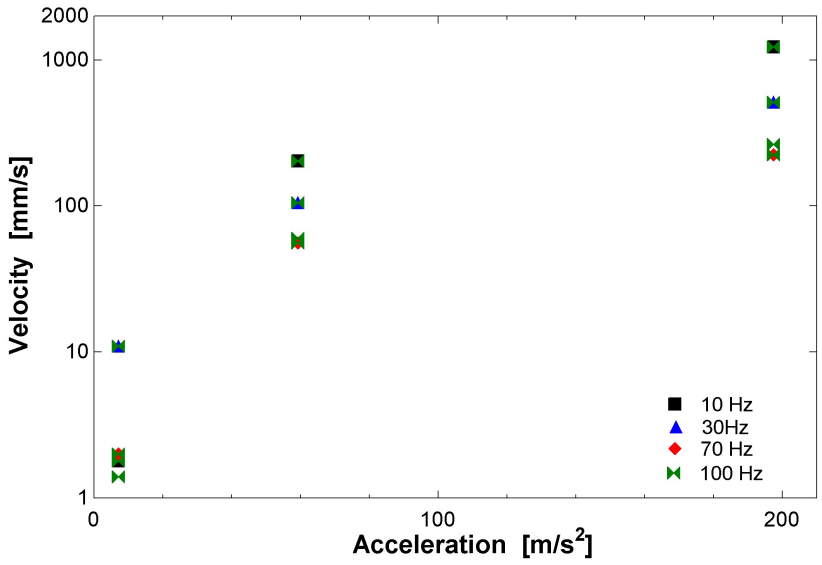

Figure 4.10 Average downward velocities for constant accelerations across different frequencies [40]

The inconsistency in average downward velocity across the different frequencies at the same acceleration shows that the velocity of the droplets is not solely determined by the acceleration. Thus, the average downward velocities of the vibrations with the same vibration amplitudes were compared, seen in Figure 4.11. The average downward velocities all have the same trend for all three amplitudes, with the velocity decreasing as the frequency decreases from 100 Hz to 10 Hz. These results are compiled in the 3D plot in Figure 4.12, demonstrating the proportional effects of amplitude and higher-order effects of frequency.

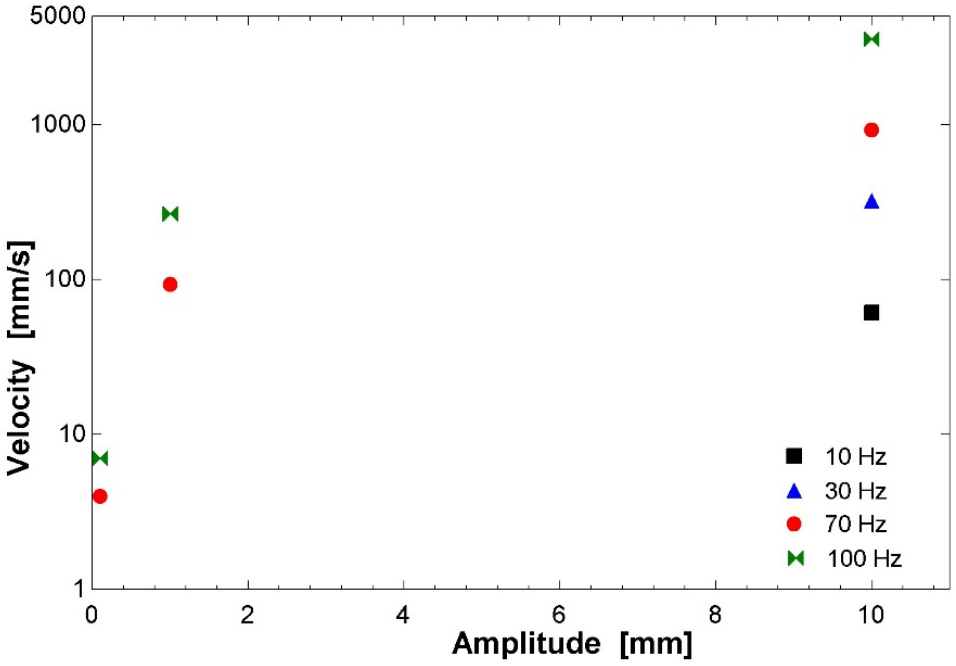

Figure 4.11 Average downward velocities for constant amplitudes across different frequencies [40]

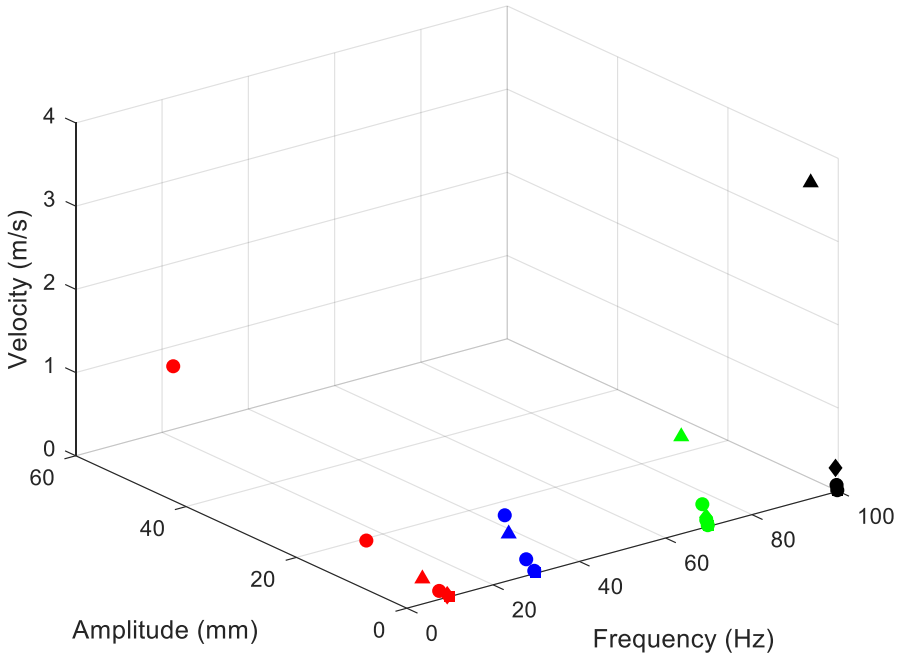

Figure 4.12 Three-dimensional plot of velocity vs amplitude and frequency [40]

4.3.3 Non-dimensional analysis

A non-dimensional study was conducted to investigate trends in droplet motion. In order to non-dimensionalize the data, the Strouhal number was calculated across the four frequencies, by using Eq. 4.11,

$$St = \frac{fD}{u} \qquad \textbf{Eq. 4.11}$$

where f is the frequency, D is the diameter, and u is the average downward velocity. The Strouhal number was plotted for the constant non-dimensionalized maximum acceleration (i.e., the maximum y-direction acceleration, a_{max} divided by gravitational acceleration, g=9.81 m/s^2); now referred to as acceleration in the remainder of this section. The Strouhal number decreases as the frequency decreases from 100 Hz to 10 Hz for the 6.02 and 20.08 G cases. For the .725 m/s2 G case, the 30 Hz case has the lowest Strouhal number instead of 10 Hz, as seen in Figure

4.13. This is likely due to the large average downward velocity caused by the proximity to resonance.

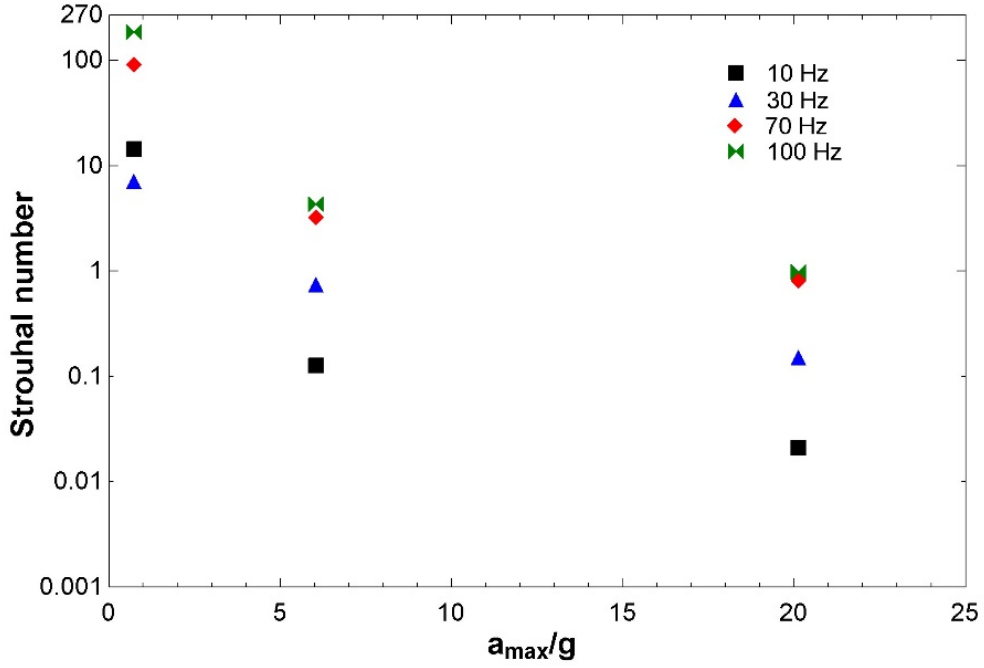

Figure 4.13 Strouhal number for constant accelerations across different frequencies [40]

Other non-dimensional parameters of interest for droplet motion include the Capillary, *Ca*, Weber, *We*, and Reynolds numbers, *Re*, given by the following equations,

$$Ca = \frac{\eta u}{\sigma} \qquad \textbf{Eq. 4.12}$$

$$We = \frac{\rho D_0 u^2}{\sigma} \qquad \textbf{Eq. 4.13}$$

$$Re = \frac{\rho u D_0}{\eta} \qquad \textbf{Eq. 4.14}$$

where η and ρ are dynamic viscosity and density of water, respectively, and D_0 is the initial diameter (i.e., 2.6 mm). Capillary, Weber, and Reynolds numbers are plotted in Figure 4.14, Figure 4.15, Figure 4.16 respectively, versus acceleration. While no clear trends emerged from the study, possible transition values from droplet ratcheting to breakup could be seen. With

breakup occurring at approximately $Ca > 0.0044$, $We > 3.6$, and $Re > 1000$. However, this are not sufficient data and not enough data points around the transition lines to determine hard cut offs.

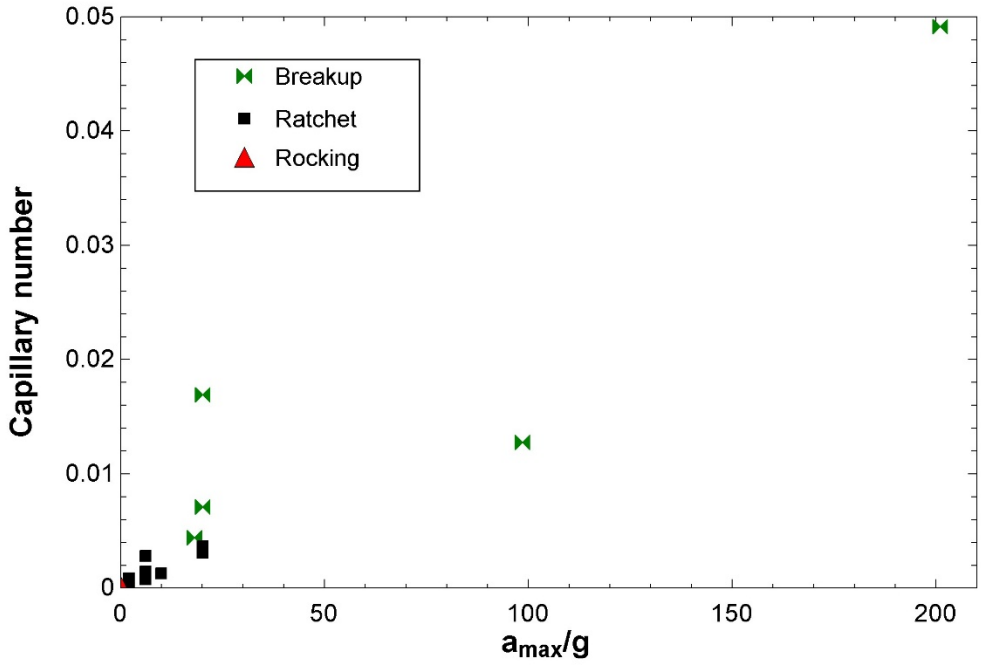

Figure 4.14 Capillary numbers for droplet motion modes (i.e., ratchet and breakup) versus non-dimensionalized acceleration on vibrating surfaces for f=10, 30, 70, and 100 Hz [40]

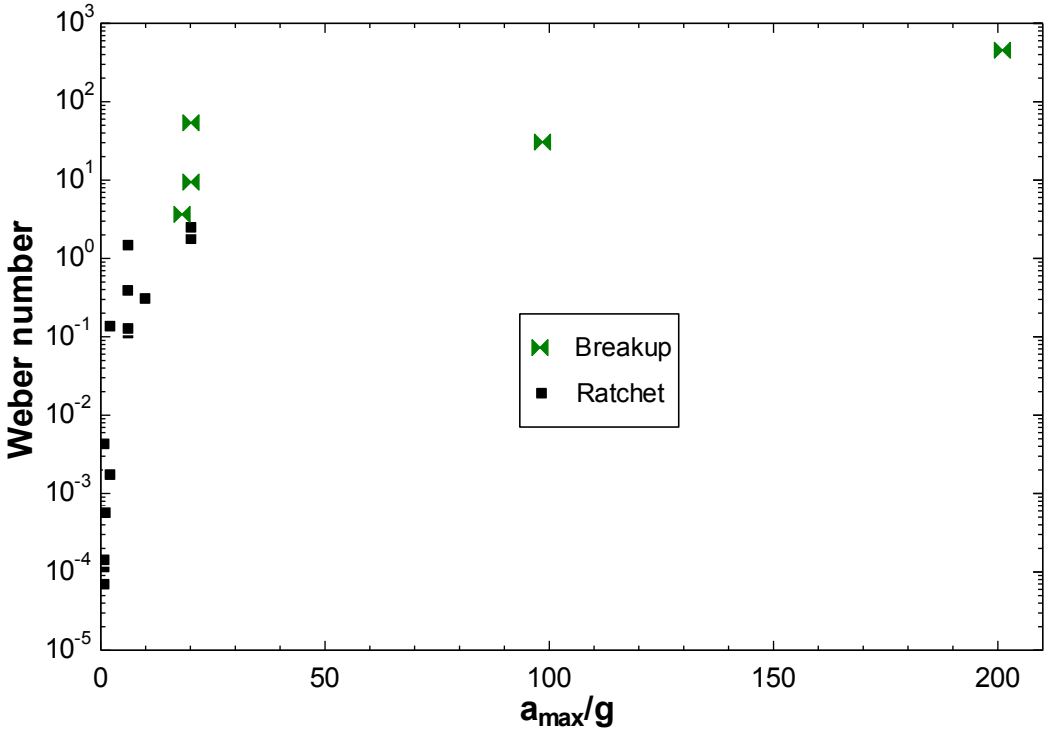

Figure 4.15 Higher Weber numbers associated with the breakup of the liquid droplet; data are for f=10, 30, 70, and 100 Hz and rocking modes are excluded from the graph [40]

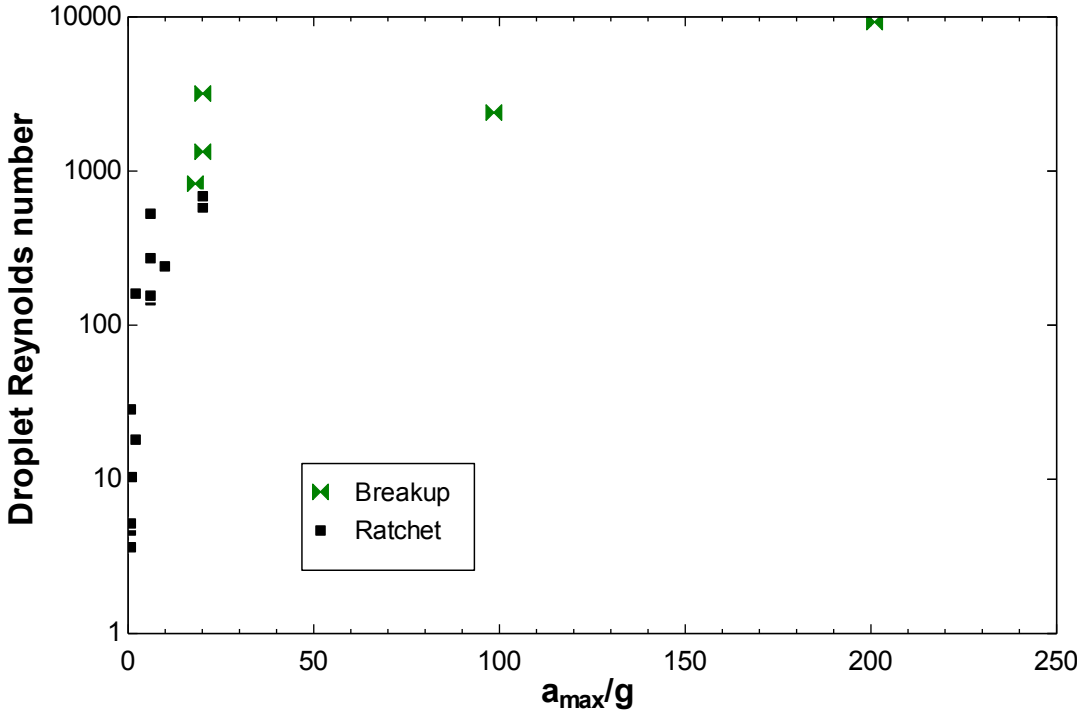

Figure 4.16 Reynolds number calculated based on initial droplet diameter with respect to non-dimensionalized acceleration; data are for f=10, 30, 70, and 100 Hz and rocking modes are excluded from the graph [40]

Chapter 5 - Condensation Results and Discussion

5.1 Visualization Data[4]

5.1.1 Vibrations' Impacts on Droplet Growth Stages

Three of the conduction experiments were conducted with vibrations of approximately 100 Hz and one stationary test was included for comparison. Nucleation was not a major focal point of improvement from the effects of vibration going into the experiments; based on the camera used, it was estimated that droplets under 50μm were not clearly visible. Figure 5.1 shows the times it took for each stage of condensation to occur. The start to observable stage is the time it took from the start of the experiment until droplets could be observed on the surface by the camera. The direct growth stage is the time it took from when the droplets were observable to when they began to coalesce with one another. The coalescence stage is the time it took from the beginning of coalescence to when the first droplet departed. The stationary film had visible droplets in the field of view after 19 minutes. However, during the vibration experiments, the droplets became visible later. This could be due to the camera not being able to focus on the vibrating droplets or the vibrations impacting nucleation. While coalescence began later on the vibrating surfaces, the time it took to coalesce into droplets with critical droplet diameters was less. Some of this may be due to the smaller size needed for droplets to depart on the vibrating surface 2-3 mm versus 7 mm on the stationary surface. However, vibrations prompt

[4] Figures and parts of this section were first published in 58. Huber, R.A., Guanes, G., Derby, M. M., *Liquid Removal through Vibrations on a Flexible Film for Condensing/Dehumidication*, in *ASHRAE 2018 Winter Conference*. 2018, American Society of Heating, Refrigeration, and Air Conditioning Engineers. and 59. Huber, R.A. and M.M. Derby. *Droplet Coalescence and Departure on a Vibrating Film During Humid Air Condensation*. in *ASME 2017 15th International Conference on Nanochannels, Microchannels, and Minichannels*. 2017. American Society of Mechanical Engineers.

droplets to move around and come into contact with their neighbors more often than the stationary droplets. As Figure 5.1 demonstrates, vibration tests one and three took around 18 minutes of coalescence before drops began to move while test two only took seven minutes for drops to begin to move. The stationary film however, took 76 minutes for a drop to move.

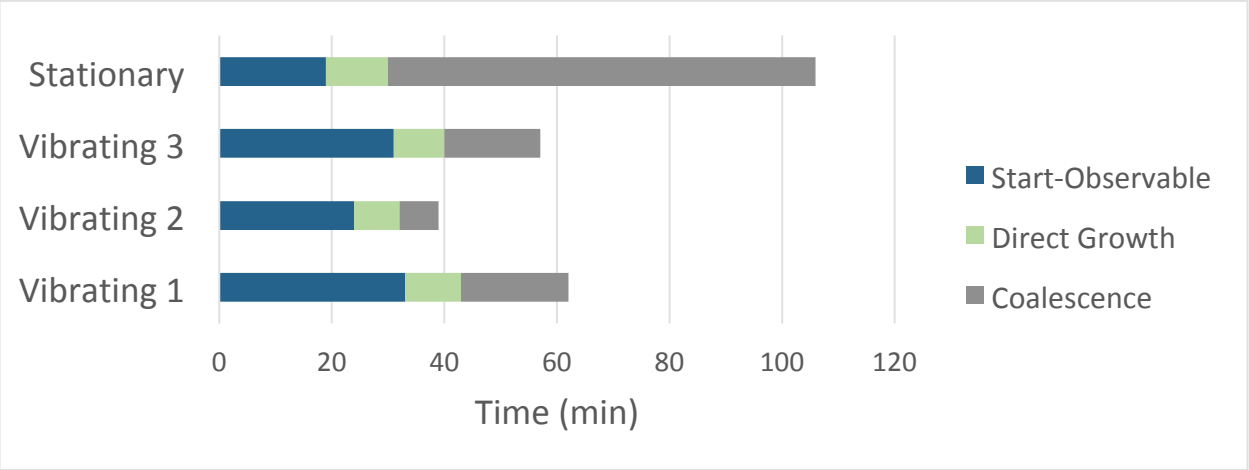

Figure 5.1 Time for each stage of droplet growth [59]

Figure 5.2 shows vibrating experiment one and the stationary test at the same time after cooling began. Even though the stationary film had about ten more minutes of time to coalesce than the vibrating film, the vibrating surface has larger drops as well as having a greater variety of droplet sizes. While the overall drop size is larger on the stationary surface, the vibrating surface increases the speed at which large droplets coalesce. Some of the droplets on the vibrating film are already beginning to depart from the film, with 2 to 5 mm diameters. The main objective of this experiment was to speed up the time it took for droplets to leave a surface. The stationary test took 115 minutes for a droplet to reach the departure diameter. The vibrating films took under 80 minutes for droplets to be able to leave the surface. Simply applying vibrations to a film allowed a new round of nucleation to begin a full 35 minutes before the stationary film would allow. Castillo et al. [31], determined that on a stationary film with relative humidity

between 45 and 50%, approximately 80 to 100 minutes elapsed before droplets departed. The difference in temperature that Castillo had 15°C where in this work it was usually around 10°C. Due to this slight temperature difference we can expect slower condensation times.

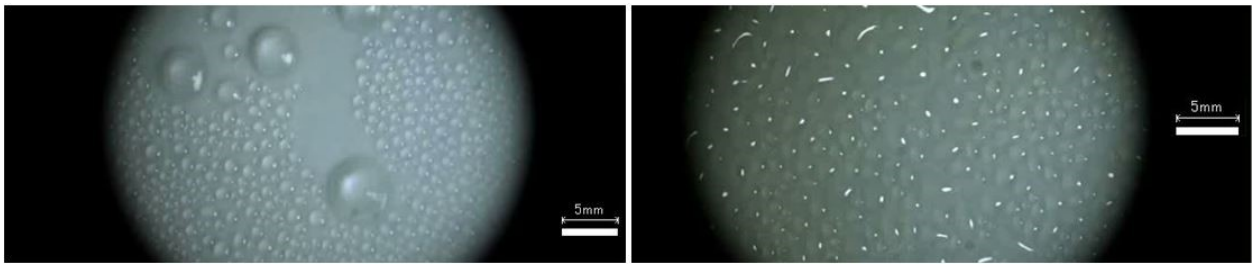

Figure 5.2 Vibrating film on the left with moving droplets and Stationary film on the right during coalescence both at 72 min [59]

Different experiments resulted in a different number of drops and times to create the droplets as can be seen in Table 5.1 The stationary test had the least amount of droplets depart, with two drops falling over the three-hour-long test. The stationary test also took the longest for a drop to fall at 115 minutes. Vibration tests 1 and 3 had a similar number of drops shed, with seven and eight, respectively. They also had a similar time when drops started to shed, around 75 minutes. The first test had the remainder of its droplets depart much quicker that the third test, with the remaining six drops departing, at 78 to 83 minutes, before the second drop departed on the third test at 83 minutes. The second vibrating test was much quicker than the other two vibrating tests, with a drop departing at 44 minutes. A possible reason for the drastic differences from the other two vibrating tests could be the location of the camera relative to the spot the cold air was hitting the surface.

Table 5.1 Time for individual droplets to reach critical diameter to depart the surface [59]

Drops	1st	2nd	3rd	4th	5th	6th	7th	8th
Vibrating 1	76.5	78.7	79.1	79.9	81.3	81.5	83.1	
Vibrating 2	43.8	50.1	58.1	58.2	59.9			
Vibrating 3	75	83.5	85.7	85.8	87.4	92.4	97.6	101.4
Stationary	115.2	181.5						

5.1.2 Vibrations' impacts on critical diameter

Stationary and vibrating experiments were conducted at each of the four environmental conditions to understand the impacts of vibrations on the condensation process. The four chamber conditions were 1) 35 °C and 60% RH, 2) 35 °C and 50% RH, 3) 30 °C and 66% RH, and 4) 30 °C and 60% RH. The test cases at 35°C 50% RH and 30°C 66% RH have around the same absolute humidity of 20 g/m^3. One life cycle of droplets was observed for each of these environmental conditions. A life cycle of a droplets is defined as time from when the cold air was applied to the surface to when the test section has produced droplets that depart the surface. Critical droplet diameters (i.e., the diameter of the drop on the horizontal axis, parallel to the ground) for each test are shown in Figure 5.3. For the vibrating droplets, droplets are circular in nature and the critical drop diameter was also a good measure of their vertical diameter as well. However, the stationary droplets were more amorphous or irregularly shaped than the circular droplets on the vibrating tests, causing their vertical diameters to be larger than their horizontal diameters. The graph shows that the critical drop diameter is larger for the stationary tests for every test condition from 5 mm (0.2 in) to 1 mm (0.04 in) for the vibrating test condition. Vibrations reduced the pinning forces, so that less mass is needed for the gravitational forces to exceed the pinning forces, thereby permitting small droplets to leave the surface.

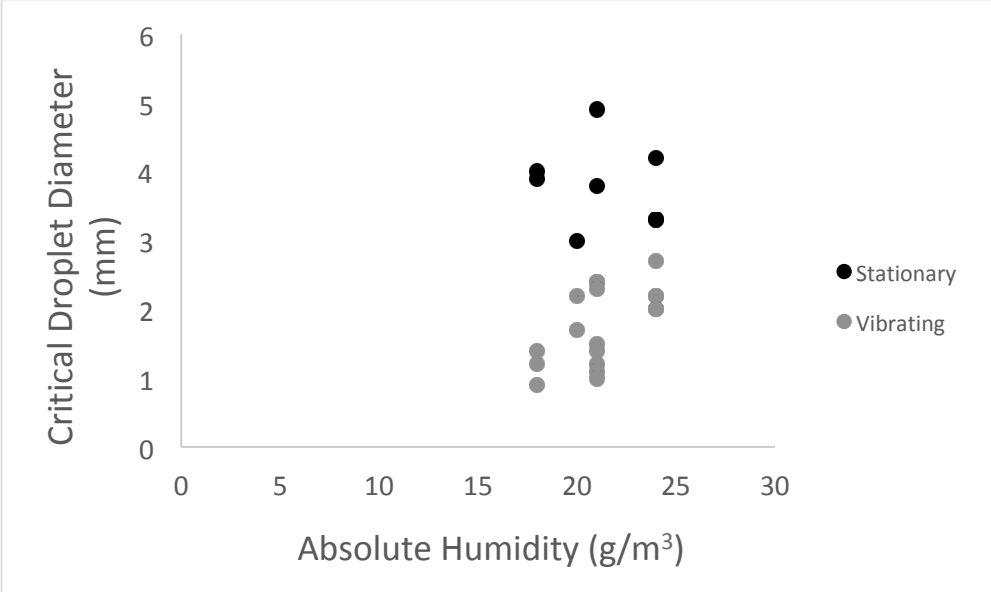

Figure 5.3 Critical droplet diameters observed [58]

The first drop to depart each test can be seen in Figure 5. This shows that not only are the departing droplets smaller for the vibrating tests, but the time it takes for droplets to depart is also shorter. The critical droplet diameters are smaller for the vibrating test. Additionally, vibrations incite droplet coalescence. During the vibrating experiments, individual droplets would shake around on the surface and these shaking droplets would collide bump into their neighboring drops and subsequently merge. This induced merging as a result of vibrations prompted smaller droplets to leave the vibrating surface in less time than was required by the gravity-driven, stationary surface.

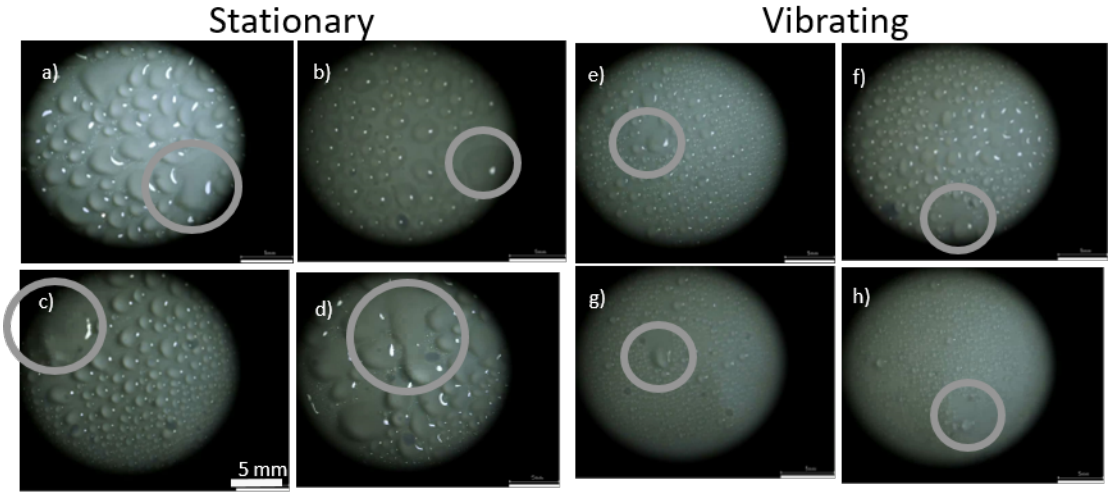

Figure 5.4 The first droplet beginning to depart. a) T=35°C 60% RH at 46 minutes, b) T=35°C 50% RH at 94 minutes, c) T=31°C 66% RH at 24 minutes d) T=30°C 60% RH at 71 minutes, e) T=35°C 60% RH at 16 minutes, f) T=35°C 50% RH at 16 minutes, g) T=31°C 66% RH [58]

5.1.3 Impacts of Vibrations and Various Ambient Conditions

Castillo et al. [31], investigated the effect of relative humidity on condensation, with ambient temperature set at 20 °C, the surface temperature set at 5 °C, and relative humidity from 45% to 70%. The experimental conditions used in this work had slightly higher ambient and surface temperatures, although the results for the stationary tests are generally in the same time frame of approximately 60 minutes, leading to good confidence in the results. Figure 5.5 Life cycle times for each ambient condition (°C and %RH) for both stationary and vibrating tests [58] shows the time taken for one life cycle of condensing droplets. The vibrations applied to the film sped up the life cycle of the droplets, and it is roughly 30 minutes, half of the time of the stationary tests. When comparing the test of same temperature, the lower humidity takes more time to complete one life cycle. For the same temperature, at lower humidity levels the stationary and vibrating tests both take at least twice as long to complete; however, the stationary case has a larger increase in the life cycle time compared to the vibration tests increase in life cycle time.

Comparing the two tests that have the same relative humidity the lower temperature test has a longer droplet life cycle than the higher temperature test. Once again, the stationary test has the largest increase in life cycle. This data show that vibrations on the condensing surface will decrease the life cycle of droplets across many cases and add to the other factors influencing condensation rate.

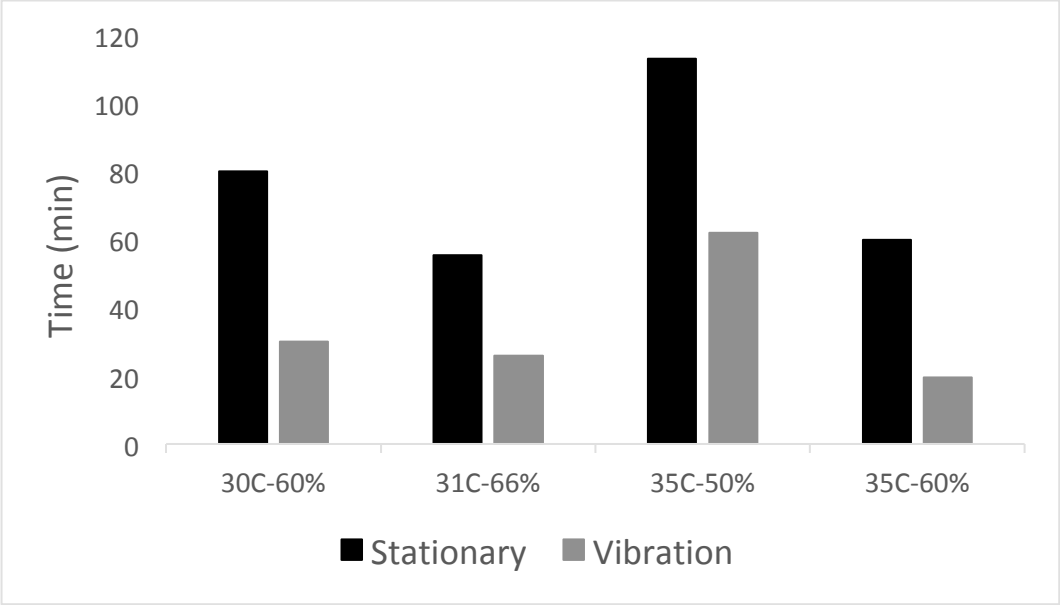

Figure 5.5 Life cycle times for each ambient condition (°C and %RH) for both stationary and vibrating tests [58]

5.2 Heat Transfer Data

5.2.1 Validation Data

Validation test were carried out by heating the plate to 30 °C while the ambient air was set to 20 °C so that no condensation could occur. This was done so that the condensation results that resulted from the apparatus could be trusted since predicting the moist air condensation heat transfer coefficients do not have established models. Since no condensation was occurring the validation tests were all on a stationary surface. The heat transfer coefficients for the heating

were calculated using Eq. 2.3 through Eq. 2.10 and compared to the Nusselt number for forced convection over a flat plate, Eq. 5.1.

$$Nu = 0.664\, Re^{1/2} Pr^{1/3} \qquad \textbf{Eq. 5.1}$$

Where *Nu* is the Nusselt number, *Re* is the Reynolds number, and *Pr* is the Prandtl number. Table 5.2 shows the experimental and calculated data. The Reynolds number was calculated by using the ambient air velocity of 4.5 m/s. The heat transfer coefficients show good agreement and are within 20% and the uncertainty bands for the measured data.

Table 5.2 Experimental and Predicted heat transfer coefficients for validation tests

Experimental HTC (W/m^2K)	Predicted HTC (W/m^2K)
32.65 ± 7.53	26.37
33.27 ± 9.45	26.52

5.2.2 Condensation Data

Heat transfer calculations, Eq. 2.3 through Eq. 2.10, were done on stationary and vibrating condensation test data to analyze if there was any enhancement from the vibrations. Five tests were run for both stationary and vibrating at a temperature set point of 40 °C and 60% RH. Although the temperature was not able to consistently be set for every test or the duration of each test the temperature and relative humidity didn't vary more than ±15% of their respective set points. The vibrations were set to have an amplitude of 0.15 mm and frequency of 170 Hz. Figure 5.6 shows the surface of the test surface for the stationary tests in a and b at 8 minutes and 9 seconds and 15 minutes and 1 second respectively while c and d show the test surface for the vibrating tests at the same time. For these test cases 8 minutes and 9 seconds is when the first droplets begin departing from the surface for the vibrating test whereas 15 minutes and 1 second

is the time the first droplet starts to depart for the stationary test. Droplets that are beginning to shed or are shedding are circled. For the stationary case, the droplet will immediately depart within a second of the frame shown below. For the vibrating cases, the droplet motion can be steadily moving downwards due to vibrations before suddenly departing making it hard to tell when the droplet has finally overcome the forces holding it on the surface.

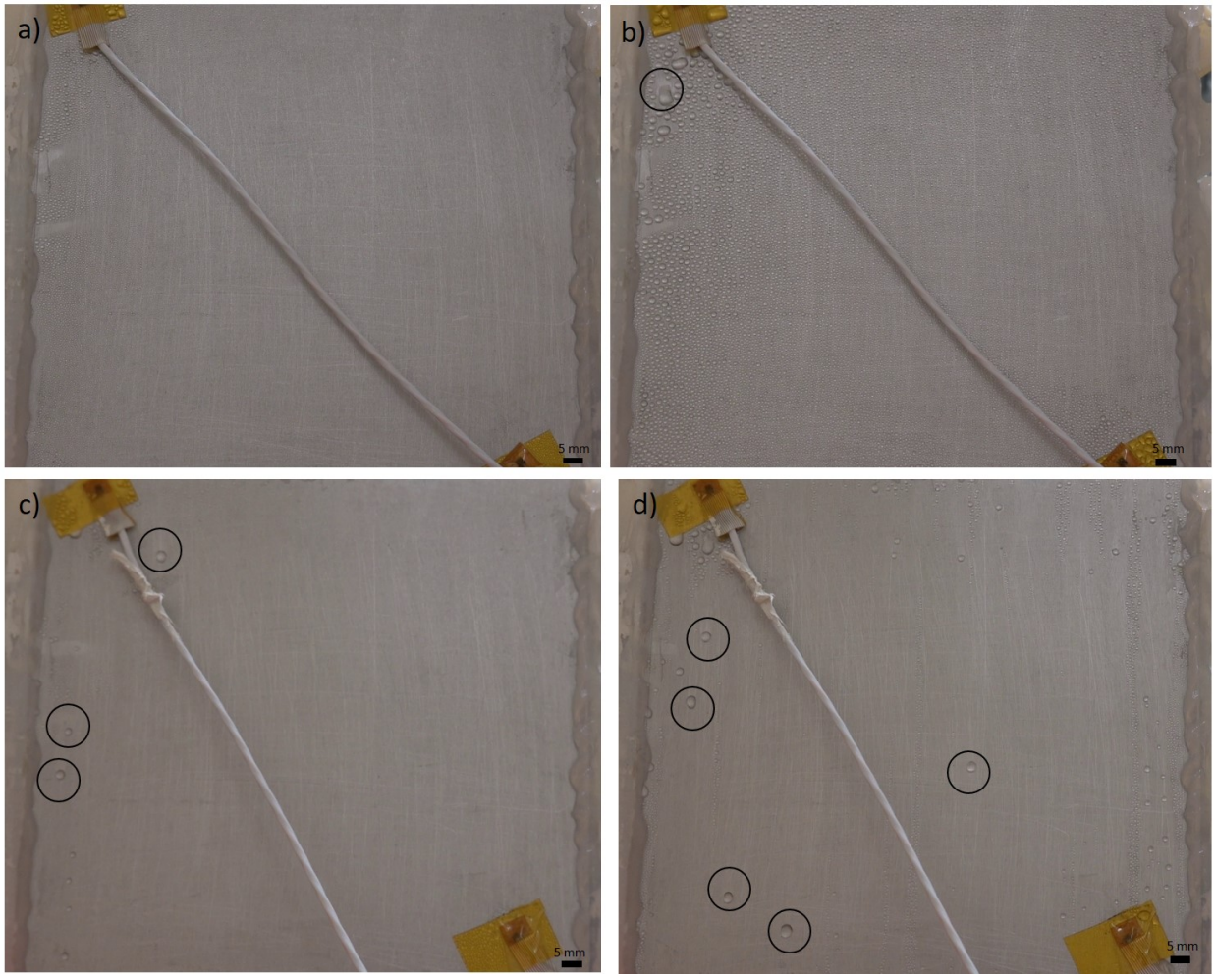

Figure 5.6 a) Stationary test at 8:09 b) Stationary test at 15:01 c) Vibrating test at 8:09 d) Vibrating test at 15:01

Figure 5.7 shows the average heat transfer coefficients for all the tests at their corresponding absolute humidity in g/m^3 and their experimental uncertainties. This figure does not show much and it is hard to tell if the vibrations enhanced the heat transfer coefficients at all.

However, the heat transfer coefficients are in similar line with values from Gu et al. This is promising since much research done on moist air condensation does not report heat transfer coefficients.

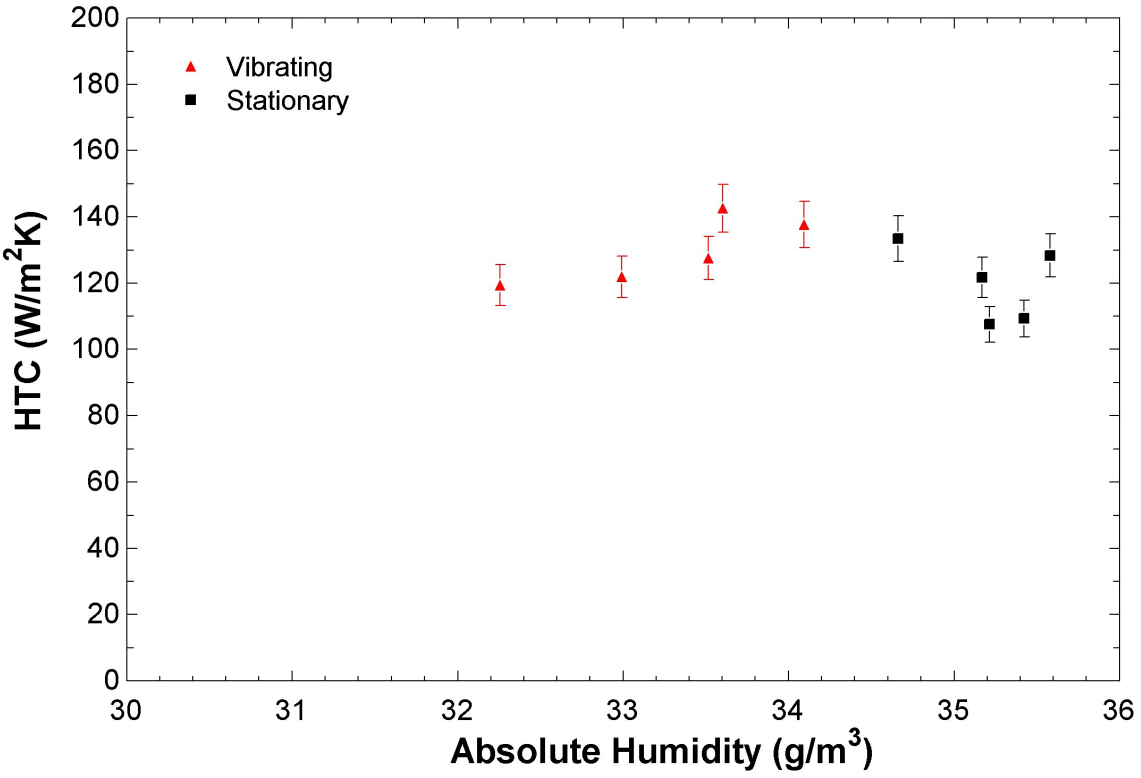

Figure 5.7 Heat transfer coefficients for stationary and vibrating dropwise condensation

Setting a null hypothesis of vibrations not enhancing heat transfer coefficients during dropwise condensation and performing a one-tailed T-test on the data returned a P value of 0.095. This means that with 90% certainty the data shows that vibrations enhance heat transfer coefficients during dropwise condensation. However, this enhancement did not amount to much for the given apparatus only increasing the mean HTC by 8%. While this is not a large increase in HTC and below the normal confidence level of 95% it is enough to show that there is promise in this area and could be further improved upon from the current method. Issues with the current apparatus and proposed solutions can be found in Section 6.2 Future Work.

Chapter 6 - Conclusions and Future Work

6.1 Conclusions

The impacts that vibrations had on individual water droplets and water droplets on a condensing surface were examined on a vertical hydrophobic surface. After visualization experiments and numerical simulations, it was determined that vibrations can cause rocking, ratchet, and ejecting motions on an individual droplet. These different motions are a product of different vibrational modes applied to the surface. During the ratchet motion, the droplets will slide down the surface when normally they would be pinned to the surface. The effects of vibrations do not solely rely on any one factor, although acceleration is the most substantial factor in determining if a droplet moves or not. For a 2.6-mm diameter droplet, it was found that accelerations between 2 m/s^2 and 7 m/s^2 were required for a water droplet to slide on the simulated hydrophobic surface. Frequency can play a major role in the velocity at which a droplet departs, due to droplets having resonance frequencies in which the forces acting on the droplet can amplify themselves. A minor change in droplet motion was observed; with the addition of various additives to water, which changed the surface tension, viscosity, and density of the water by varying degrees.

The impacts of vibrations on dropwise condensation heat transfer from moist air visually demonstrated that vibration droplets spend a shorter time coalescing than stationary droplets (i.e., 10 minutes versus 70 minutes). Water droplets depart at a smaller diameter (e.g., 2 mm versus 7 mm) and sooner in the condensation process (e.g., 50 minutes versus 105 minutes). Even if the water droplets do not depart, vibrating droplets are still rocking on the surface, which promotes

coalescence with other droplets. The heat transfer data measured from moist air condensation tests shows that there is probable cause that vibrations may cause a small enhancement (e.g., 8%) to the heat transfer coefficient during condensation from moist air. Further work needs to be done in order to strengthen this conclusion and determine if further enhancement is possible.

6.2 Future Work

The modest heat transfer coefficient enhancement due to vibrations is most likely due to the small difference in heat transfer values. One hypothesis for this is that the current rate of condensation from moist air is simply too low (e.g., air-side resistances dominate). If the rate of condensation were faster, the vibrations would shed even more droplets, which would clear a larger area for new, smaller droplets to form. This would also prompt the smaller droplets to grow due to direct condensation much faster and increase the heat transfer. To accomplish this, it is necessary to increase the sub-cooling of the condensing surface by lowering the inlet temperature of the working fluid. Another option would be to increase the relative humidity of the chamber closer to 100% RH, although that would require a different environmental chamber.

Another hypothesis is that the area being cleared by the droplets isn't a large enough percentage to make a larger difference. Flow observations noted the majority of condensation taking place on the left half of the plate where cooling air temperatures are lower. Switching the working fluid to water would allow for a lower temperature difference across the plate, allowing for a more even condensation rate, but would pose challenges to measuring the heat transfer rate (e.g., very inlet-to-exit low temperature differences). Another possibility is to change the geometry by decreasing the length of the condensing surface to increase the percentage of area the droplets are clearing.

Chapter 7 - Bibliography

1. Maupin, M.A., et al., *Estimated use of water in the United States in 2010*. 2014, US Geological Survey.

2. Ghosh, R., T.K. Ray, and R. Ganguly, *Cooling tower fog harvesting in power plants–A pilot study.* Energy, 2015. **89**: p. 1018-1028.

3. Dietz, C., et al., *Visualization of droplet departure on a superhydrophobic surface and implications to heat transfer enhancement during dropwise condensation.* Applied physics letters, 2010. **97**(3): p. 033104.

4. Lee, J.B., et al. *Wettability Effect on Droplet Growth Behaviors During Dropwise Condensation*. in *ASME 2015 International Mechanical Engineering Congress and Exposition*. 2015. American Society of Mechanical Engineers.

5. Badr, L., G. Boardman, and J. Bigger, *Review of water use in US thermoelectric power plants.* Journal of Energy Engineering, 2012. **138**(4): p. 246-257.

6. Macknick, J., et al., *Operational water consumption and withdrawal factors for electricity generating technologies: a review of existing literature.* Environmental Research Letters, 2012. **7**(4): p. 045802.

7. Meldrum, J., et al., *Life cycle water use for electricity generation: a review and harmonization of literature estimates.* Environmental Research Letters, 2013. **8**(1): p. 015031.

8. Bustamante, J.G., A.S. Rattner, and S. Garimella, *Achieving near-water-cooled power plant performance with air-cooled condensers.* Applied Thermal Engineering, 2016. **105**: p. 362-371.

9. Sun, Y., Z. Guan, and K. Hooman, *A review on the performance evaluation of natural draft dry cooling towers and possible improvements via inlet air spray cooling.* Renewable and Sustainable Energy Reviews, 2017. **79**: p. 618-637.

10. Kong, Y., et al., *Direct dry cooling system through hybrid ventilation for improving cooling efficiency in power plants.* Applied Thermal Engineering, 2017. **119**: p. 254-268.

11. Kong, Y., et al., *Combined air-cooled condenser layout with in line configured finned tube bundles to improve cooling performance.* Applied Thermal Engineering, 2019.

12. Zavaragh, H.G., M.A. Ceviz, and M.T.S. Tabar, *Analysis of windbreaker combinations on steam power plant natural draft dry cooling towers.* Applied Thermal Engineering, 2016. **99**: p. 550-559.

13. Wagner, M.J. and C. Kutscher. *The impact of hybrid wet/dry cooling on concentrating solar power plant performance*. in *ASME 2010 4th International Conference on Energy Sustainability*. 2010. American Society of Mechanical Engineers.

14. Al-Ibrahim, A.M. and A. Varnham, *A review of inlet air-cooling technologies for enhancing the performance of combustion turbines in Saudi Arabia.* Applied thermal engineering, 2010. **30**(14-15): p. 1879-1888.

15. Alkhedhair, A., et al., *Numerical simulation of water spray for pre-cooling of inlet air in natural draft dry cooling towers.* Applied Thermal Engineering, 2013. **61**(2): p. 416-424.

16. Harto, C.B., et al., *Updating GETEM to Include a Hybrid Cooling Option and Local Climate Variability for Binary Power Plants.*

17. He, S., et al., *A review of wetted media with potential application in the pre-cooling of natural draft dry cooling towers.* Renewable and Sustainable Energy Reviews, 2015. **44**: p. 407-422.

18. Ibrahim, T.K., M. Rahman, and A.N. Abdalla, *Improvement of gas turbine performance based on inlet air cooling systems: A technical review.* International journal of physical sciences, 2011. **6**(4): p. 620-627.

19. Punwani, D.V., et al., *A hybrid system for combustion turbine inlet air cooling at a cogeneration plant in Pasadena, Texas/Discussion.* ASHRAE Transactions, 2001. **107**: p. 875.

20. Smrekar, J., J. Oman, and B. Širok, *Improving the efficiency of natural draft cooling towers.* Energy Conversion and Management, 2006. **47**(9-10): p. 1086-1100.

21. Wei, H., et al., *Performance of a novel natural draft hybrid cooling system with serial airside heat exchange.* Applied Thermal Engineering, 2019. **147**: p. 361-370.

22. Sun, Y., et al., *Spray cooling system design and optimization for cooling performance enhancement of natural draft dry cooling tower in concentrated solar power plants.* Energy, 2019. **168**: p. 273-284.

23. Al-Ansary, H.A., J.A. Orfi, and M.E. Ali, *Impact of the use of a hybrid turbine inlet air cooling system in arid climates.* Energy conversion and management, 2013. **75**: p. 214-223.

24. Brunet, P., J. Eggers, and R. Deegan, *Vibration-induced climbing of drops.* Physical review letters, 2007. **99**(14): p. 144501.

25. Daniel, S., M.K. Chaudhury, and P.-G. De Gennes, *Vibration-actuated drop motion on surfaces for batch microfluidic processes.* Langmuir, 2005. **21**(9): p. 4240-4248.

26. Quéré, D., M.-J. Azzopardi, and L. Delattre, *Drops at rest on a tilted plane.* Langmuir, 1998. **14**(8): p. 2213-2216.

27. Dong, L., A. Chaudhury, and M. Chaudhury, *Lateral vibration of a water drop and its motion on a vibrating surface.* The European Physical Journal E, 2006. **21**(3): p. 231-242.

28. Mettu, S. and M.K. Chaudhury, *Motion of liquid drops on surfaces induced by asymmetric vibration: role of contact angle hysteresis.* Langmuir, 2011. **27**(16): p. 10327-10333.

29. Rose, J.W., *Dropwise condensation theory.* International Journal of Heat and Mass Transfer, 1981. **24**: p. 191-194.

30. Rose, J., *Condensation heat transfer.* Heat and mass transfer, 1999. **35**(6): p. 479-485.

31. Castillo, J.E., J.A. Weibel, and S.V. Garimella, *The effect of relative humidity on dropwise condensation dynamics.* International Journal of Heat and Mass Transfer, 2015. **80**: p. 759-766.

32. Leach, R., et al., *Dropwise condensation: experiments and simulations of nucleation and growth of water drops in a cooling system.* Langmuir: the ACS journal of surfaces and colloids, 2006. **22**(21): p. 8864.

33. Barati, S.B., et al., *Investigation spatial distribution of droplets and the percentage of surface coverage during dropwise condensation.* International Journal of Thermal Sciences, 2018. **124**: p. 356-365.

34. Sokuler, M., et al., *The softer the better: fast condensation on soft surfaces.* Langmuir, 2009. **26**(3): p. 1544-1547.

35. Mu, C., et al., *Effects of surface topography of material on nucleation site density of dropwise condensation.* Chemical engineering science, 2008. **63**(4): p. 874-880.

36. Beysens, D. and C. Knobler, *Growth of breath figures.* Physical review letters, 1986. **57**(12): p. 1433.

37. Rose, J., *Dropwise condensation theory.* International Journal of Heat and Mass Transfer, 1981. **24**(2): p. 191-194.

38. Huber, R., et al. *Impacts of water quality on vibration-induced water droplet removal for cooling tower water capture*. in *ASTFE Digital Library*. 2019. Begel House Inc.

39. Schmitz, E., *Impacts of industrial water composition on Salicornia in a hydroponic system*, in *Biological and Agricultural Engineering*. 2018, Kansas State University.

40. Huber, R.A., et al., *Vibration-enhanced droplet motion modes: Simulations of rocking, ratcheting, ratcheting with breakup, and ejection.* Journal of Fluids Engineering, 2019. **141**(7).

41. Noblin, X., A. Buguin, and F. Brochard-Wyart, *Vibrations of sessile drops.* The European Physical Journal Special Topics, 2009. **166**(1): p. 7-10.

42. Noblin, X., R. Kofman, and F. Celestini, *Ratchetlike motion of a shaken drop.* Physical review letters, 2009. **102**(19): p. 194504.

43. Hao, L. and P. Cheng, *Lattice Boltzmann simulations of liquid droplet dynamic behavior on a hydrophobic surface of a gas flow channel.* Journal of power sources, 2009. **190**(2): p. 435-446.

44. Fan, J., M. Wilson, and N. Kapur, *Displacement of liquid droplets on a surface by a shearing air flow.* Journal of colloid and interface science, 2011. **356**(1): p. 286-292.

45. Seevaratnam, G., et al., *Laminar flow deformation of a droplet adhering to a wall in a channel.* Chemical Engineering Science, 2010. **65**(16): p. 4523-4534.

46. Chen, X., et al., *Droplet ejection and sliding on a flapping film.* AIP Advances, 2017. **7**(3): p. 035014.

47. Yang, A.-S. and W.-M. Tsai, *Ejection process simulation for a piezoelectric microdroplet generator.* Journal of fluids engineering, 2006. **128**(6): p. 1144-1152.

48. Bao, Y.B. and J. Meskas, *Lattice Boltzmann method for fluid simulations.* Department of Mathematics, Courant Institute of Mathematical Sciences, New York University, 2011.

49. Kang, X., W. Tang, and S. Liu, *Lattice Boltzmann Method for Simulating Disturbed Hemodynamic Characteristics of Blood Flow in Stenosed Human Carotid Bifurcation.* Journal of Fluids Engineering, 2016. **138**(12): p. 121104.

50. Murdock, J.R., A. Ibrahim, and S.-L. Yang, *An Efficient Method of Generating and Characterizing Filter Substrates for Lattice Boltzmann Analysis.* Journal of Fluids Engineering, 2018. **140**(4): p. 041203.

51. Wafik, A., et al., *Experimental and Numerical Investigations Using Lattice Boltzmann Method to Study Shedding Vortices in an Unsteady Confined Flow Around an Obstacle.* Journal of Fluids Engineering, 2015. **137**(10): p. 101203.

52. Yuan, P. and L. Schaefer, *A thermal lattice Boltzmann two-phase flow model and its application to heat transfer problems—part 1. Theoretical foundation.* Journal of Fluids Engineering, 2006. **128**(1): p. 142-150.

53. Yuan, P. and L. Schaefer, *A thermal lattice Boltzmann two-phase flow model and its application to heat transfer problems—part 2. Integration and validation.* Journal of fluids engineering, 2006. **128**(1): p. 151-156.

54. Bhardwaj, S., et al., *Analysis of droplet dynamics in a partially obstructed confinement in a three-dimensional channel.* Physics of Fluids, 2018. **30**(10): p. 102102.

55. XFlow, S., *XFlow 2018 Theory Guide*. 2018.

56. Shih, T.-H., et al., *A generalized wall function.* 1999.

57. Perez, M., et al., *Oscillation of liquid drops under gravity: Influence of shape on the resonance frequency.* EPL (Europhysics Letters), 1999. **47**(2): p. 189.

58. Huber, R.A., Guanes, G., Derby, M. M., *Liquid Removal through Vibrations on a Flexible Film for Condensing/Dehumidication*, in *ASHRAE 2018 Winter Conference*. 2018, American Society of Heating, Refrigeration, and Air Conditioning Engineers.

59. Huber, R.A. and M.M. Derby. *Droplet Coalescence and Departure on a Vibrating Film During Humid Air Condensation*. in *ASME 2017 15th International Conference on Nanochannels, Microchannels, and Minichannels*. 2017. American Society of Mechanical Engineers.

Appendix A - Heat Transfer Data

Table A.1 Calculated and measured data from condensation experiments

Test	Vibrations	Water (mL)	h (W/m2K)	Uncertainty (W/m2/K)	Q (W)	Uncertainty (W)
1	N	15	107.6	5.38	30.74	0.7
2	N	17	109.32	5.49	29.92	0.69
3	N	18	121.69	6.12	29.82	0.69
4	Y	18	142.54	7.25	31.29	0.71
5	N	18	128.34	6.52	30	0.69
6	Y	5	119.38	6.16	27.34	0.67
7	Y	20	137.65	7.01	30.89	0.71
8	Y	18	121.9	6.2	29.55	0.69
9	Y	17	127.54	6.47	30.17	0.69
10	N	8	133.48	6.86	29.15	0.69

Table A.2 Averaged measured plate temperatures and ambient conditions

Test	Tp (°C)	Ta (°C)	Td (°C)	RH (%)	Abs Hum (g/m3)
1	29.8	42.1	33.4	62.33	35.21379309
2	30.2	42	33.5	63.01	35.42277485
3	30.23	40.78	33.3	66.46	35.16933587
4	31.51	40.96	32.5	62.93	33.60102301
5	30.62	40.68	33.5	67.57	35.57900854
6	29.81	39.67	31.7	64.43	32.25381358
7	30.34	40.01	32.7	66.95	34.09182571
8	29.26	39.7	32.1	65.8	32.9893025
9	29.88	40.06	32.4	65.65	33.51367357
10	30.71	40.11	33	67.73	34.66215801

Table A.3 Mass flow rates for each channel

Test	m1 (kg/s)	m2 (kg/s)	m3 (kg/s)	m4 (kg/s)	m5 (kg/s)
1	0.000865	0.000961	0.000875	0.000923	0.000682
2	0.000865	0.000961	0.000875	0.000923	0.000692
3	0.000875	0.000942	0.000884	0.000923	0.000692
4	0.000884	0.000952	0.000884	0.000942	0.000721
5	0.000884	0.000942	0.000884	0.000923	0.000702
6	0.000894	0.000961	0.000884	0.000932	0.000644
7	0.000884	0.000952	0.000904	0.000961	0.000682
8	0.000894	0.000961	0.000904	0.000961	0.000625
9	0.000865	0.000952	0.000884	0.000932	0.000721
10	0.000884	0.000961	0.000894	0.000932	0.000615

Table A.4 Average inlet temperatures for each channel

Test	Inlet 1 (°C)	Inlet 2 (°C)	Inlet 3 (°C)	Inlet 4 (°C)	Inlet 5 (°C)
1	15.76576295	15.67963686	15.35553812	15.12118044	15.43929077
2	15.63246279	14.9310362	15.37100116	15.03273385	15.50013901
3	16.11121803	15.4979215	16.27715368	15.89222968	16.1552111
4	16.1272811	15.9954055	16.15897535	15.66741457	16.07443412
5	16.05534659	15.79859475	16.65424958	15.85406035	16.2798449
6	16.3969035	16.81523497	18.45848112	16.85602797	16.87771469
7	16.04895765	15.55966592	16.37464921	15.73693313	16.24052828
8	15.54631061	14.78213659	15.87949302	15.32049441	15.68033743
9	15.95748922	15.22408956	16.52166527	15.70088413	16.20437503
10	17.01414741	16.73763176	17.70299659	16.87747467	17.12511668

Table A.5 Average exit temperatures for each channel

Test	Exit 1 (°C)	Exit 2 (°C)	Exit 3 (°C)	Exit 4 (°C)	Exit 5 (°C)
1	21.2296806	21.10204214	22.79889611	23.32061531	26.23764555
2	21.03225224	20.66507414	22.43083898	22.86749146	25.61733594
3	21.30197282	21.35614868	23.26109903	23.72744161	26.21287101
4	21.20195324	21.75660754	23.54492321	24.07390649	26.4389626
5	21.60104428	21.672978	23.31997716	23.76219487	26.19380513
6	22.1085021	22.29956783	23.76971469	24.1271049	26.25721189
7	21.12812037	21.42327668	23.61066676	23.92044051	26.47446475
8	20.49877961	20.79535726	22.85960698	23.02807849	25.62881564
9	21.20570501	21.25535209	23.18801036	23.53923678	26.29080912
10	22.35119522	22.57531929	24.46275242	24.6278099	27.03699943

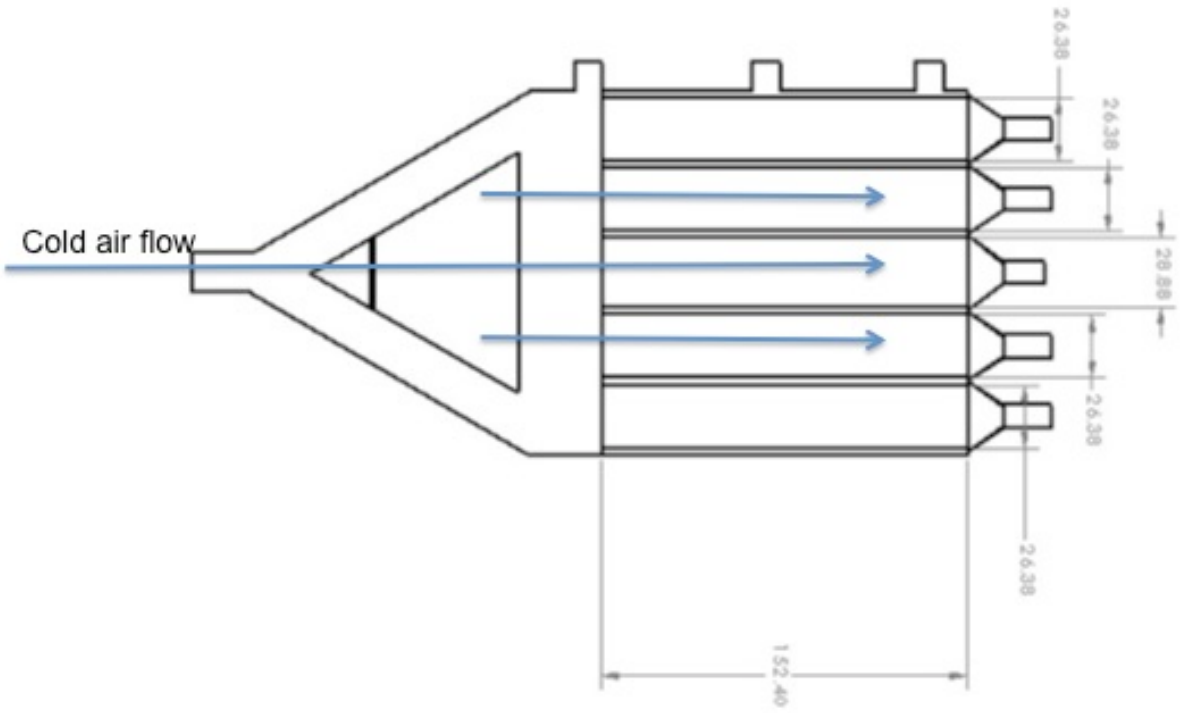

Figure A.1 Drawing of 3D printed part with channel measurements